Monthly Notices
of the
ROYAL ASTRONOMICAL SOCIETY

MNRAS **465,** 123–148 (2017)
Advance Access publication 2016 October 12

doi:10.1093/mnras/stw2605

The SAMI Galaxy Survey: asymmetry in gas kinematics and its links to stellar mass and star formation

J. V. Bloom,[1,2]★ L. M. R. Fogarty,[1,2] S. M. Croom,[1,2] A. Schaefer,[1,2] J. J. Bryant,[1,2,3] L. Cortese,[4] S. Richards,[1,2,3] J. Bland-Hawthorn,[1] I-T. Ho,[5] N. Scott,[1,2] G. Goldstein,[6] A. Medling,[7] S. Brough,[3] S.M. Sweet,[7] G. Cecil,[8] A. López-Sánchez,[3,6] K. Glazebrook,[9] Q. Parker,[10,3,6] J. T. Allen,[1,2] M. Goodwin,[3] A. W. Green,[3] I. S. Konstantopoulos,[3,11] J. S. Lawrence,[3] N. Lorente,[3] M. S. Owers[3,6] and R. Sharp[7]

[1]*Sydney Institute for Astronomy, School of Physics, University of Sydney, NSW 2006, Australia*
[2]*ARC Centre of Excellence for All-Sky Astrophysics (CAASTRO), Australia*
[3]*Australian Astronomical Observatory, PO Box 915, North Ryde, NSW 1670, Australia*
[4]*International Centre for Radio Astronomy Research, The University of Western Australia, 35 Stirling Hwy, Crawley, WA 6009, Australia*
[5]*Institute for Astronomy, University of Hawaii, 2680 Woodlawn Drive, Honolulu, HI 96822, USA*
[6]*Department Physics and Astronomy, Macquarie University, NSW 2109, Australia*
[7]*Research School for Astronomy and Astrophysics. Mount Stromlo Observatory, ANU, Cotter Road Weston Creek, ACT 2611, Australia*
[8]*Department Physics and Astronomy University of North Carolina Chapel Hill, NC 27599, USA*
[9]*Centre for Astrophysics and Supercomputing, Swinburne University of Technology, Hawthorn, VIC 3122, Australia*
[10]*Department of Physics, The University of Hong Kong, Hong Kong*
[11]*Envizi Group Suite 213, National Innovation Centre, Australian Technology Park, 4 Cornwallis Street, Eveleigh, NSW 2015, Australia*

Accepted 2016 October 7. Received 2016 September 27; in original form 2015 September 7

ABSTRACT

We study the properties of kinematically disturbed galaxies in the Sydney-AAO Multi-object Integral field spectrograph (SAMI) Galaxy Survey using a quantitative criterion, based on kinemetry (Krajnović et al.). The approach, similar to the application of kinemetry by Shapiro et al., uses ionized gas kinematics, probed by H α emission. By this method, 23 ± 7 per cent of our 360-galaxy sub-sample of the SAMI Galaxy Survey are kinematically asymmetric. Visual classifications agree with our kinemetric results for 90 per cent of asymmetric and 95 per cent of normal galaxies. We find that stellar mass and kinematic asymmetry are inversely correlated and that kinematic asymmetry is both more frequent and stronger in low-mass galaxies. This builds on previous studies that found high fractions of kinematic asymmetry in low-mass galaxies using a variety of different methods. Concentration of star formation and kinematic disturbance are found to be correlated, confirming results found in previous work. This effect is stronger for high-mass galaxies ($\log(M_*) > 10$) and indicates that kinematic disturbance is linked to centrally concentrated star formation. Comparison of the inner (within $0.5R_e$) and outer H α equivalent widths of asymmetric and normal galaxies shows a small but significant increase in inner equivalent width for asymmetric galaxies.

Key words: methods: data analysis – techniques: imaging spectroscopy – galaxies: evolution – galaxies: interactions – galaxies: kinematics and dynamics– galaxies: structure.

1 INTRODUCTION

Hierarchical galaxy formation, in which dark matter haloes form through a series of mergers, is central to Λcold dark matter cosmology (Peebles 1982; Cole et al. 2008; Neistein & Dekel 2008). It is well established from *N*-body simulations (e.g. Mayer et al. 2007; Stewart et al. 2009) that the rate of both halo and galaxy mergers should vary with redshift, but the precise details are not yet fully understood. There are discrepancies between theory and observation. For example, major mergers are known from theory to transform discy galaxies into thick, flared, bulge-dominated

★ E-mail: jessica.bloom@sydney.edu.au

© 2016 The Authors
Published by Oxford University Press on behalf of the Royal Astronomical Society

systems, which we would then expect to dominate the local Universe. We instead see a large proportion of thin, discy systems at low redshift (Mihos & Hernquist 1994; Zucca et al. 2006).

Previous studies of galaxy disturbance have used images to either visually or quantitatively calculate the degree of disturbance within galaxies (e.g. Burkey et al. 1994; Lotz, Primack & Madau 2004; De Propris et al. 2007; Darg et al. 2010). Visual identification of close pairs was used to determine merger rates in the Sloan Digital Sky Survey (SDSS; Ellison et al. 2013) and Galaxy And Mass Assembly (GAMA) Survey (Robotham et al. 2014) samples. Structural analysis has also been used (Casteels et al. 2014). These methods have been employed to determine merger rates in the nearby (Darg et al. 2010) and high-redshift (Conselice et al. 2003a) universe. These merger rates are, however, not always consistent. For example, the merger rate calculated by close pair counting in Lin et al. (2004) is an order of magnitude lower than that found by Conselice et al. (2003a). The discrepancy has been noted in the literature and efforts have been made to reconcile different results from different methods, such as in Lotz et al. (2011).

Despite the success of these approaches, they have limitations: purely visual analyses are difficult (although not impossible) to quantify (Casteels et al. 2013) and quantitative morphological techniques can be influenced by Hubble type and are restricted in the range of asymmetries to which they are sensitive. This is the case in the Concentration/Asymmetry/Smoothness system (Conselice, Chapman & Windhorst 2003b). The Asymmetry parameter can be influenced by the presence of spiral arms, which can mask the effects of minor asymmetries (Conselice et al. 2003b). Further, at high redshift, galaxies may be photometrically asymmetric but kinematically regular due to features such as clumpy star formation (Glazebrook 2012).

Recent technological advances have revolutionized the reach of spectroscopy. Previously, the majority of spectroscopic measurements were taken with a single fibre or slit (e.g. York et al. 2000; Percival et al. 2001; Driver et al. 2009). For extended sources, such as galaxies, this approach is highly vulnerable to aperture effects and it is difficult to gather information about spatial variation across the source. Integral field spectroscopy (IFS) solves this problem by taking spectra at various positions across the object, opening up new scientific possibilities.

Instruments such as K-band Multi Object Spectrograph (Sharples et al. 2013), Fibre Large Array Multi Element Spectrograph (Pasquini et al. 2002) and Spectrograph for INtegral Field Observations in the Near Infrared (Eisenhauer et al. 2003) have demonstrated the usefulness of IFS. Surveys such as Spectroscopic Imaging survey in the Near-infrared with SINFONI (SINS) (Shapiro et al. 2008) and ATLAS^{3D} (Cappellari et al. 2011) have used IFS technology to spatially resolve and measure disturbances in the kinematics of high- and low-redshift galaxies, respectively. The ATLAS^{3D} and SINS surveys differ in redshift and scale, but they have both demonstrated that the 2D kinematics of galaxies can be used to effectively classify disturbed galaxies at various epochs (Shapiro et al. 2008). We also note the use of 'simulated IFU' techniques by Kutdemir et al. (2008). Both SINS and ATLAS^{3D} used monolithic instruments, which involve taking IFS measurements for each object individually.

The Sydney-AAO Multi-object Integral field spectrograph (SAMI) is a multiplexed spectrograph, able to produce sample sizes into the thousands of galaxies on a much shorter time-scale than a single IFS instrument (Croom et al. 2012). We here demonstrate how the large sample of IFS data in the SAMI Galaxy Survey can be used to determine an asymmetric fraction (i.e. fraction of galaxies classified as asymmetric) from gas kinematics, using a method based on kinemetry. Further, we show that classification methods based on kinematics are more robust in distinguishing interacting galaxies within the SAMI Galaxy Survey sample than methods based on quantitative morphology. We finally present results showing links between kinematic asymmetry, concentration of star formation and stellar mass.

In Section 2, we give a brief overview of the SAMI instrument and SAMI Galaxy Survey sample, outlining the data reduction pipeline and production of emission line maps, as well as characterizing the sub-sample used in this work. In Section 3, we describe the kinematic classification method used to identify kinematically asymmetric galaxies, as well as a visual classification scheme used to calibrate the results from kinemetry. Section 4 shows the results of using kinemetry to identify perturbed galaxies and compares them directly with results from quantitative morphology. Section 5 contains a comparison of our results to those from high-redshift studies. Sections 6 and 7 show relationships between kinematic asymmetry, stellar mass and star formation rate (SFR). Section 8 briefly discusses the active galactic nuclei (AGN) in our sample. We conclude in Section 9.

2 THE SAMI GALAXY SURVEY

The SAMI Galaxy Survey will consist of 3400 galaxies across a range of stellar masses and environments, within $0.004 < z < 0.095$ (Croom et al. 2012). The increased size of the survey sample is possible within a relatively short time frame because the SAMI instrument can take observations of up to 12 galaxies at a time (plus one calibration star), greatly increasing the ease with which large samples of IFS data can be obtained.

2.1 The SAMI

The SAMI instrument takes integral field spectra for multiple objects using innovative imaging fibre bundles, called hexabundles (Bryant et al. 2011). The SAMI hexabundles consist of 61 optical fibres, with each core subtending ∼1.6 arcsec on sky, so that the total bundle diameter is ∼15 arcsec. Each bundle has a physical size <1 mm and a filling factor of 75 per cent (Bryant et al. 2012). 13 bundles are manually plugged into a field plate, installed at the prime focus of the Anglo–Australian Telescope (AAT), and a fibre cable then feeds to the double-beamed AAOmega spectrograph. AAOmega is configured with a dichroic splitting the light at 5700 Å with the 580 V blue arm grating having a wavelength range of 3700–5700 Å and the 1000 R red arm grating having a wavelength range of 6300–7400 Å. This gives resolutions of $R \sim 1730$ in the blue arm and $R \sim 4500$ in the red arm (Croom et al. 2012). All objects are observed with both arms of the spectrograph. Measurements used in this work are of the Hα line, which is observed using the high-resolution arm of the spectrograph.

2.2 Sample selection and data reduction

The 3400 galaxies of the SAMI Galaxy Survey were selected from the GAMA survey (Driver et al. 2009), supplemented by eight galaxy clusters. The GAMA galaxies selected consist of both group and field galaxies and were chosen to reflect a broad range in stellar mass, in accordance with the science drivers of the SAMI Galaxy Survey. The GAMA galaxies lie on the celestial equator at RA ∼ 9, 12 and 15 h, covering a total of 144 deg^2. The GAMA survey provides a uniform and highly complete (∼99 per cent), *r*-band flux

limited survey of three large representative regions of the sky (Liske et al. 2015).

From the GAMA survey galaxies, those with unreliable redshifts or magnitudes were rejected. The final sample consists of four stellar mass, volume-limited sub-samples, along with additional dwarf galaxies at low redshift (Bryant et al. 2015).

In order to provide more complete spatial coverage, each galaxy in the sample is observed in a series of seven exposures. The individual exposures are combined to produce two data cubes per galaxy, one for each arm of the spectrograph, with 0.5 arcsec spatial pixels (spaxels).

All reduction of data taken using the AAOmega spectrograph at the AAT uses the software 2DFDR.[1] The 2DFDR package conducts all steps of the data reduction up to the production of wavelength calibration and sky-subtracted spectra (Sharp et al. 2015).

The first stage of data reduction using 2DFDR is the subtraction of bias and dark frames. In order to ensure good extraction of spectra from the 2D data frame, it is necessary to accurately map the positions and profiles of the fibres across the detectors. This is accomplished using a fibre flat-field frame, which is taken using an illumination of a white spot on the inside of the AAT dome. Wavelength calibration is then performed, using frames of standard CuAr arc-lamp exposures. Twilight exposures are used to measure the relative throughput between all fibres in the instrument. Finally, there are 26 dedicated sky fibres in the SAMI instrument. These fibres are set to blank sky positions for each field, to measure the sky spectrum, which can then be subtracted from all spectra.

The next steps of the data reduction process, the flux calibration correction and correction for telluric absorption are independent of 2DFDR and are conducted using an external software suite, written in PYTHON (Allen et al. 2014). For the flux calibration, spectrophotometric standard stars are observed, when possible, on the same night as the galaxy observations. Secondary standard stars are observed simultaneously with the galaxies and are used to derive a correction in the telluric bands at 6850–6960 and 7130–7360 Å. Data cubes are produced with regular 0.5 arcsec^2 spaxels. Some spatial resolution is lost when convolving 1.6 arcsec fibres with 0.5 arcsec spaxels, because the flux in each output spaxel is taken as the mean of the flux in each input fibre, with weightings given by the fractional overlap of the fibre with the spaxel. To regain some of the lost resolution, a 0.8 arcsec diameter fibre footprint is used to calculate the overlaps, a drizzle-like process that was initially developed to re-sample high-resolution imaging from *Hubble Space Telescope*/WPFC2 (Fruchter & Hook 2002). The final product is a pair of data cubes per galaxy, one for each arm of the spectrograph, with multiple extensions. The extensions contain, respectively, the flux, variance, weight and covariance data cubes. A full explanation of the data reduction process can be found in Sharp et al. (2015).

Due to the re-sampling process used to make the data cubes, the noise in neighbouring spaxels is correlated. This effect is negligible for spaxels spaced more than ∼2.5 spaxels apart. A full explanation of how covariance is handled in SAMI Galaxy Survey data can be found in Sharp et al. (2015).

2.3 LZIFU and data products

LZIFU is an Interactive Data Language (IDL) spectral fitting pipeline, designed to perform flexible emission line fitting in IFS data cubes. It works by fitting and then removing the continuum emission in each spaxel by using simple stellar population (SSP) models (Ho et al. 2014, 2016). LZIFU uses the penalized pixel-fitting routine, PPXF (Cappellari & Emsellem 2004) to do the continuum fit. We use theoretical SSP models, assuming Padova isochrones of solar metallicity and 18 ages (Delgado et al. 2005). After the continuum emission is removed, LZIFU models user-assigned emission lines as Gaussian profiles and then performs a bounded value non-linear least-squares fit. This is done using IDL's Levenberg–Marquardt least-squares method (Markwardt 2009), with LZIFU automatically establishing reasonable initial guesses for the wavelength of emission lines. Users have the choice to model individual emission line as either 1-, 2- or 3-component Gaussians, describing possible different kinematic components. We use 1-component fits in this work.

The key data products from the LZIFU pipeline are 2D emission line strength and kinematic maps (showing the kinematics of gas in the galaxy, both velocity and velocity dispersion), for user-assigned lines, with error maps. For a more detailed explanation of the LZIFU pipeline, see Ho et al. (2014).

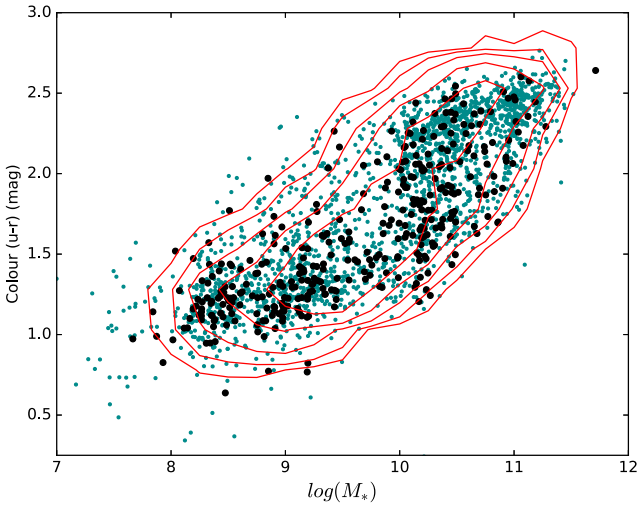

Figure 1. We show colour and stellar mass for the entire GAMA Survey sample (log-spaced red contours) SAMI Galaxy Survey sample (blue points) and the sample used in this work (black dots). Our sample is evenly distributed within the main SAMI Galaxy Survey sample. The data used were taken from the GAMA Data Release 2 catalogues ApMatchedPhotom (Hill et al. 2011) and StellarMasses (Taylor et al. 2011).

2.4 Selecting and characterizing the sample

This work uses the first 451 galaxies to be processed through the LZIFU pipeline. We took the velocity and velocity dispersion maps generated by the H α fit from LZIFU and applied an S/N cut of 10 to the H α emission map. If, after applying the cut, there were fewer than 200 spaxels remaining in the flux map, out of an original ∼1225 spaxels, the galaxy was excluded from the sample (the average being ∼450 spaxels remaining). This was to avoid problems fitting severely discontinuous, low S/N maps. After the above cuts were performed, there remained a sample of 360 galaxies, which forms the basis of our study.

Fig. 1 shows the distribution of the rest-frame $(u - r)$ colour–stellar mass for our sample (black points), the full SAMI Galaxy Survey sample (blue points) and the parent GAMA survey sample (log-spaced red contours). For ease of comparison, the GAMA survey sample in these figures has been restricted to $z \leq 0.095$. Likewise, Fig. 2 shows dust obscuration-corrected SFR against stellar

[1] http://www.aao.gov.au/science/software/2dfdr

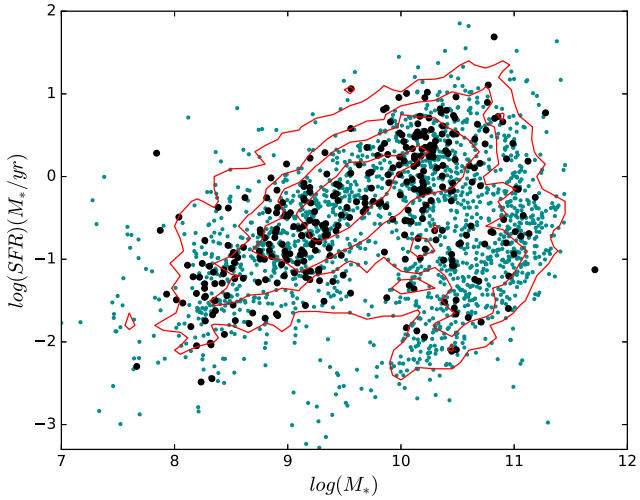

Figure 2. We show SFR against stellar mass for the GAMA Survey sample (log-spaced red contours), SAMI Galaxy Survey sample (blue points) and our sample (black dots). The Hα kinemetry sample has a slight bias against galaxies that fall off the main sequence of star formation, due to the cut in Hα S/N. The data used were taken from the GAMA Data Release 2 catalogues StellarMasses (Taylor et al. 2011) and SpecLineSFR (Hopkins et al. 2013).

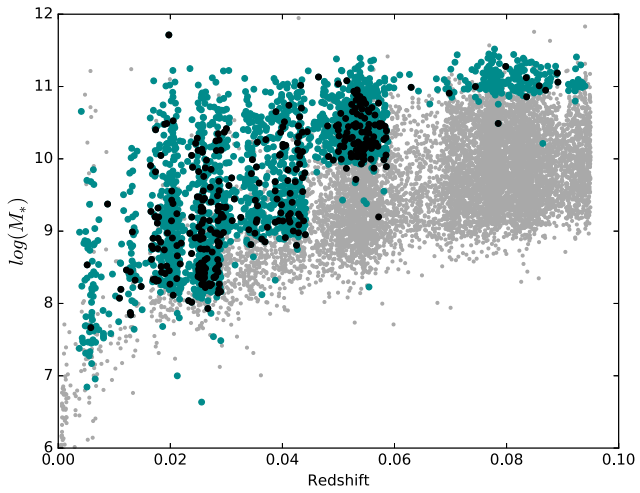

Figure 3. We show redshift and stellar mass for the GAMA Survey sample (grey points), SAMI Galaxy Survey sample (blue points) and our sample (black dots). Our sample is evenly distributed within the main SAMI Galaxy Survey sample. The data used were taken from the GAMA Data Release 2 catalogues StellarMasses (Taylor et al. 2011) and SpecLineSFR (Hopkins et al. 2013).

mass and Fig. 3 shows redshift against stellar mass, with the GAMA Survey sample in grey. Finally, Figs 4 and 5 show histograms of the colour and specific star formation rate (SSFR) for both samples. SFRs are calculated from the luminosity of the hydrogen Balmer lines. This is because the Balmer emission-line luminosity is directly proportional to the total ionizing flux of the stars in H II regions of star-forming galaxies. Medians for the stellar mass, colour and SFR for the full SAMI Galaxy Survey Sample and our sample and the results of two-sample Kolmogorov–Smirnov tests between the samples are provided in Table 1. Our sample shows a slight bias towards bluer galaxies with low stellar masses and higher SFR (see Table 1), as is to be expected when applying an Hα emission-based

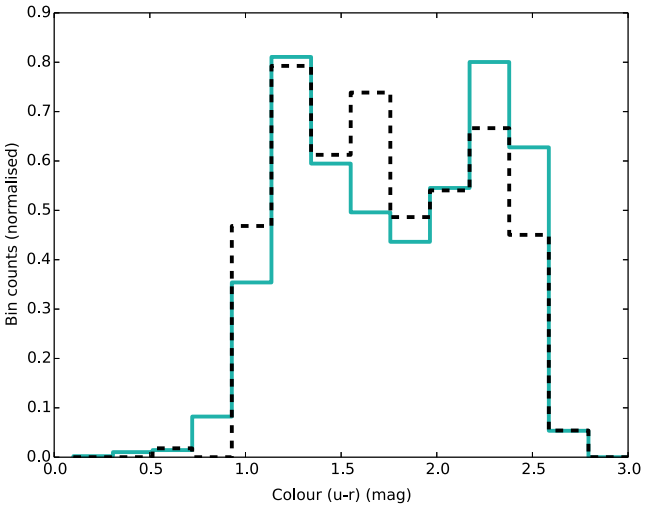

Figure 4. We show a normalized histogram of the colours in the SAMI Galaxy Survey sample (blue) and the sample used in this work (black, dashed). The data used were taken from the GAMA Data Release 2 catalogue SpecLineSFR (Hopkins et al. 2013).

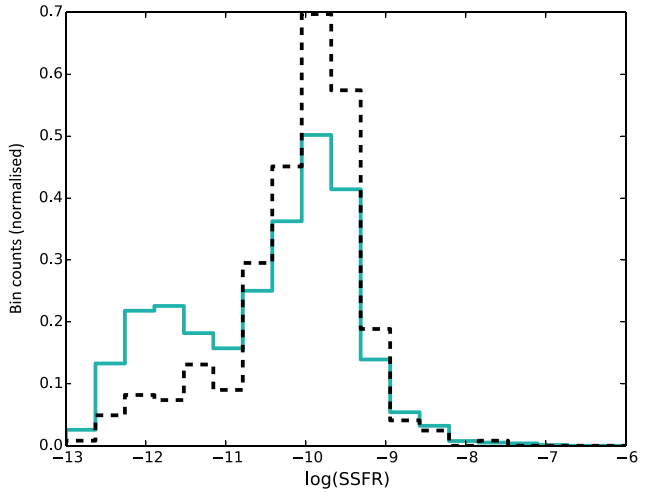

Figure 5. We show a normalized histogram of the specific SFR in the SAMI Galaxy Survey sample (blue) and the sample used in this work (black, dashed). The data used were taken from the GAMA Data Release 2 catalogues SpecLineSFR (Hill et al. 2011) and StellarMasses (Taylor et al. 2011).

Table 1. This table shows the median stellar mass, colour and SFR values for the SAMI Galaxy Survey sample and the sub-sample used in this work and the results of two-sample Kolmogorov–Smirnov tests for colour, mass and SFR. There is a slight bias towards blue, high-SFR, low-stellar mass galaxies in our sample, as is to be expected after performing an Hα S/N cut. We nevertheless cover the full parameter space (see Figs 1–3). The uncertainty we quote in the table is the statistical error on the median, rather than the uncertainty on SFR or colour for individual galaxies.

Sample	$\log(M_*)$	$(u-r)$ Colour	log(SFR)
SAMI Galaxy Survey sample	10.04 ± 0.024	1.77 ± 0.012	-0.66 ± 0.023
Our sample	9.70 ± 0.056	1.53 ± 0.028	-0.51 ± 0.053
2KS test p-value	6.15×10^{-6}	2.70×10^{-10}	0.021

S/N cut. Despite the slight bias, we cover the full parameter space (see Figs 1–3).

3 USING KINEMETRY TO QUANTIFY KINEMATIC ASYMMETRY

3.1 The kinemetry algorithm

Kinemetry is an extension of photometry to the higher order moments of the line-of-sight velocity distribution (LOSVD).[2] It was developed as a means to quantify asymmetries in stellar velocity (and velocity dispersion) maps. These anomalies may be caused by internal disturbances or by external factors, namely interactions (Krajnović et al. 2006).

The method works by modelling kinematic maps as a sequence of concentric ellipses, with parameters defined by the galaxy centre, kinematic position angle (PA) and ellipticity. It is possible to fit the latter two parameters within kinemetry or to determine them by other means and exclude them from the fitting procedure. For each ellipse, the kinematic moment is extracted and decomposed into the Fourier series:

$$K(a,\psi) = A_0(a) + \sum_{n=1}^{N}(A_n(a)\sin(n\psi) + B_n(a)\cos(n\psi)), \quad (1)$$

where ψ is the azimuthal angle in the galaxy plane and a is the ellipse semimajor axis length. Points along the ellipse perimeter are sampled uniformly in ψ, making them equidistant in circular projection. The series can be expressed more compactly, as (Krajnović et al. 2006):

$$K(a,\psi) = A_0(a) + \sum_{n=1}^{N} k_n(a)\cos[n(\psi - \phi_n(a))], \quad (2)$$

with the amplitude and phase coefficients (k_n, ϕ_n) defined as:

$$k_n = \sqrt{A_n^2 + B_n^2} \quad (3)$$

and

$$\phi_n = \arctan\left(\frac{A_n}{B_n}\right). \quad (4)$$

The moment maps for both velocity and velocity dispersion can thus be described by the geometry of the ellipses and power in the coefficients k_n of the Fourier terms as a function of a (Krajnović et al. 2006).

The velocity field of a completely normal, rotating disc would be entirely contained in the $\cos(\psi)$ term of equation (2), with zero power in the higher order modes, since the velocity peaks at the galaxy major axis and goes to zero along the minor axis. As a result, the power in the B_1 term represents circular motion, with deviations carried in the other coefficients. Fig. 6 shows results of kinemetric fitting to the Hα velocity maps of a normal and an asymmetric galaxy in our sample. For the normal galaxy (top), GAMA567545, all the power is in the first-order moment (k_1), whereas the asymmetric galaxy (bottom), GAMA628993, has significant power in the higher order modes ($k_3 + k_5$).

Analogously to the velocity field, a map of the velocity dispersion field of a perfectly normal rotating disc would have all power in the A_0 term (i.e. radial dispersion gradient; Krajnović et al. 2006).

[2] The kinemetry code is written in IDL, and can be found at http://davor.krajnovic.org/idl/ (Krajnović et al. 2006).

The velocity dispersion field is an even moment of the LOSVD and therefore its kinemetric analysis reduces to traditional surface photometry.

Kinemetry contains routines to fit the PA and ellipticity of the input kinematic fields. These inbuilt routines were used on the high S/N data fields from the ATLAS^{3D} survey. Similarly to the SINS survey (Shapiro et al. 2008), we found that the lower S/N of the SAMI Galaxy Survey fields, compared to ATLAS^{3D} data, led to unstable fits to these parameters. We used the PA and ellipticity from the single Sérsic fits to the SDSS *r*-band images in the GAMA Survey DR2 catalogue SersicCat (Kelvin et al. 2012). This is a reasonable step for disturbance measures because, for kinematically normal rotating galaxies, the photometric and kinematic PA should agree. This is not the case for galaxies with misaligned kinematic and photometric PAs. However, we find that galaxies with misaligned PAs are generally classified as visually asymmetric (see Section 3.3).

3.2 Using kinemetry to measure kinematic asymmetry

We perform kinemetry on the Hα velocity and velocity dispersion maps for all 360 galaxies in our sample. Following work on the SINS survey (Shapiro et al. 2008), we calculate radial kinematic asymmetry values for the velocity and velocity dispersion fields of each galaxy, respectively:

$$v_{\rm asym} = \frac{k_{3,v} + k_{5,v}}{2k_{1,v}} \sigma_{\rm asym} = \frac{k_{2,\sigma} + k_{4,\sigma}}{2k_{1,v}}, \quad (5)$$

We have slightly modified the method of Shapiro et al. (2008) that fit all moments (odd and even) when calculating both velocity and velocity dispersion asymmetry:

$$v_{\rm asym,SINS} = \frac{k_{2,v} + k_{3,v} + k_{4,v} + k_{5,v}}{4k_{1,v}} \quad (6)$$

$$\sigma_{\rm asym,SINS} = \frac{k_{1,\sigma} + k_{2,\sigma} + k_{3,\sigma} + k_{4,\sigma} + k_{5,\sigma}}{5k_{1,v}}. \quad (7)$$

They did this because they were specifically looking for the signatures of major mergers, which produce extremely disturbed velocity fields, with power in all higher order moments (Shapiro et al. 2008). Due to the comparatively small amplitude of the kinematic asymmetries in our sample, we found the asymmetry contributions of even moments to velocity asymmetry to be negligible (see velocity fields of GAMA618993 in Fig. 6 for an example) and similarly for the contributions of odd moments to the velocity dispersion asymmetry. Accordingly, we used only odd moments for the velocity fields and the even moments for the velocity dispersion, as was done for ATLAS^{3D} data (Krajnović et al. 2011).

Krajnović et al. (2006) note that, when studying the velocity dispersion of the stellar component of the galaxy, it is appropriate to normalize over the zeroth moment of the velocity dispersion. We, however, follow Shapiro et al. (2008) in normalizing both quantities over the velocity (k_1) rather than the velocity dispersion, because the velocity dispersion of the gas component of a galaxy is extremely sensitive to shocks and other features. This makes normalizing to the rotation curve (the first moment of the velocity) a more reliable choice, as it is not as sensitive to these features, but is sensitive to the potential.

To determine the centre of the kinematic maps used in this analysis, we fit a 2D Gaussian to the SAMI Galaxy Survey *r*-band continuum flux maps and took the centroid of the location of the 25 brightest spaxels in a 6 × 6 pixels area around the centre of the fitted Gaussian. We did not use the Hα emission maps because they

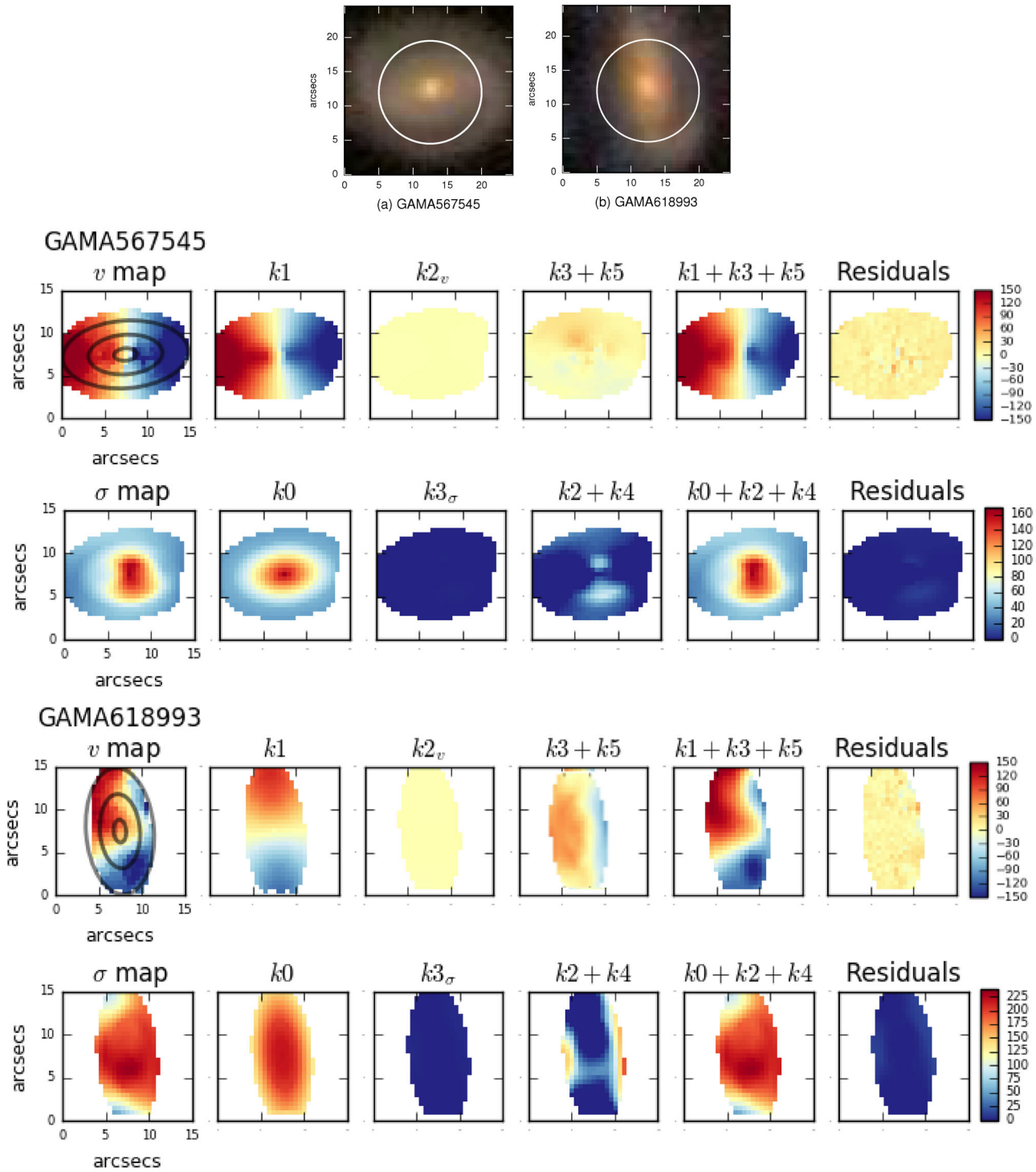

Figure 6. The input data and fitted kinemetric models for the velocity (v) and σ fields of a morphologically normal galaxy, GAMA567545 (a, top), and a morphologically asymmetric galaxy, GAMA618993 (b, bottom), with *gri* SDSS images. For each galaxy, the top row of plots shows the v models. The leftmost panels are the observed SAMI Hα v fields, with the ellipses fit by kinemetry overplotted. The PA and ellipticity of the ellipses were fit using photometry from the GAMA Survey DR2 catalogue. The second panels show the first-order model, $k1$, i.e. the rotating disc component. The rotating disc model of the normal galaxy is almost identical to the data, indicating that the first component is all that is needed to fit the data for that galaxy, unlike the asymmetric galaxy. The second-order moment, designated $k2_v$, is shown in the third panel. For both galaxies, the second-order moment is close to zero, indicating that there is little 'spillover' from the odd into the even moments. The fourth panel explicitly shows the contrast between the galaxies, with the normal galaxy having little power in the higher order modes (k_3, k_5), whereas the asymmetric galaxy has significant power. The fifth plots are of the combined $k_1 + k_3 + k_5$ models for both galaxies and the sixth panel shows the residuals of the fit from the data. The second row of plots for each galaxy shows the σ models. The first plots are the σ fields, followed by the zeroth-order moment model, $k0$. The third-order σ moment, designated as $k3_\sigma$, is shown in the third panel. Analogous to $k2_v$, there is minimal power in these modes. The higher order σ models are shown fourth and the fifth panel shows the full σ model, followed by the residuals. Note that v values in the colour bars are given in km s^{-1}.

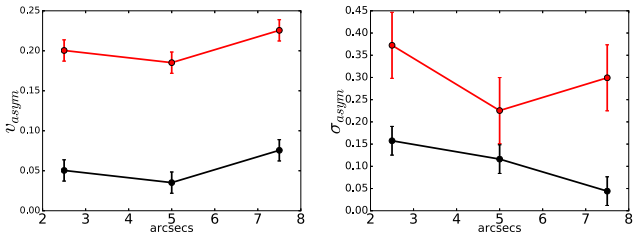

Figure 7. We show the values of $v_{\rm asym}$ (left) and $\sigma_{\rm asym}$ (right), with 1σ errors, at the positions of the semimajor radii of the fitted ellipses for an asymmetric (red, GAMA618993) and non-asymmetric (black, GAMA567545) galaxy. It can clearly be seen that the velocity and velocity dispersion asymmetry values for the asymmetric galaxy are significantly higher than those of the normal galaxy. These are the same two galaxies shown in Fig. 6.

contain clumps of star formation and other features, which make determining the centre from these maps potentially unreliable.

In order to accommodate the effects of covariance outlined in Section 2.2, we altered the kinemetry fitting routine, such that the spacing between ellipses was constrained to be $\geq$2.5 arcsec. The effective covariance diameter is $\sim$ 2.5 arcsec, so this ensures that data points used by adjacent ellipses are independent of each other. The 1σ errors on $v_{\rm asym}$ and $\sigma_{\rm asym}$ were then bootstrapped to produce the errors on $\overline{v_{\rm asym}}$ and $\overline{\sigma_{\rm asym}}$. The bootstrapping involved 100 iterations of adding random noise to the velocity and velocity dispersion fields and then recalculating the median of $v_{\rm asym}$ and $\sigma_{\rm asym}$. The final values for the errors on $\overline{v_{\rm asym}}$ and $\overline{\sigma_{\rm asym}}$ are taken from the scatter in the results of the iterations. Because of the enforced separation between ellipses, we only fit across three kinemetric ellipses for each galaxy (see Fig. 6). This does entail the possibility of losing detail, as small kinematic asymmetries may be lost 'between' successive ellipses. It is also possible that small features identified in the morphological classification in Section 3.3 may not be detected using this method. However, due to covariance, a more finely sampled kinematic fit would not increase the accuracy of our results. The qualitative nature of the visual classification means that we cannot quantitatively define a lower limit for the size of features that caused a galaxy to be classified as 'definitely asymmetric'. However, the process focused on large-scale features, such as tidal tails.

In Fig. 7, $v_{\rm asym}$ and $\sigma_{\rm asym}$ are plotted at the semimajor radii of each of the fitted ellipses for a visually normal and an asymmetric galaxy (the same galaxies as shown in Fig. 6). We see that the visually asymmetric galaxy (in red) has consistently higher kinematic asymmetry than the visually normal galaxy.

We take the median of $v_{\rm asym}$ and $\sigma_{\rm asym}$ over all ellipses (relative to the centre of the continuum emission), so that each galaxy's total kinemetric asymmetry can be expressed as the combination of $\overline{v_{\rm asym}}$ and $\overline{\sigma_{\rm asym}}$. Fig. 8 shows $\overline{\sigma_{\rm asym}}$ against $\overline{v_{\rm asym}}$ for the whole sample and for three mass bins. A discussion of the relationship between stellar mass and $\overline{v_{\rm asym}}$ can be found in Section 6. As in Shapiro et al. (2008), it will be useful to define a cutoff on this plane, above which galaxies may be considered kinematically asymmetric. Given that both $\overline{\sigma_{\rm asym}}$ against $\overline{v_{\rm asym}}$ form continuous distributions, it is not immediately obvious, based purely on kinematics, where to draw such a cutoff. Accordingly, we use visual classification to provide a guide.

3.3 Visually classifying asymmetric galaxies

The 360 galaxies in our sample were morphologically classified visually by members of the team, using *gri* composite images from the SDSS DR10 catalogue (Ahn et al. 2014). The SDSS DR10 catalogue has sufficient depth and spatial resolution to show the large-scale features relevant to our work. The median seeing, defined as the full width at half-maximum of the point spread function, in the SDSS sample is 1.43 arcsec in the *r* band. This is much smaller than the median effective radius of galaxies in the SAMI Galaxy Survey sample, 4.4 arcsec (Bryant et al. 2015). The features that define morphological asymmetry for this paper (e.g. double cores and large tidal tails) are larger than the seeing in the SDSS DR10 images. The SDSS DR10 images have been previously successfully used to identify large-scale features such as mergers in Galaxy Zoo (Darg et al. 2010; Casteels et al. 2013).

Of course, visual classification is a qualitative approach and vulnerable to bias or error. We compensated for this by having multiple people classify each galaxy, with an average of five individuals classifying each galaxy.

The categories for classification were (with quoted instructions for classification into each group and number of galaxies sorted into each category):

(i) normal: 'No evidence of interaction. These galaxies are almost completely smooth and symmetrical.' 246 galaxies;

(ii) definitely visually asymmetric: 'These galaxies do not have to be major merger remnants, but are nevertheless clearly distinguishable from normal/slightly/possibly asymmetric galaxies. They might have evidence of a double core, extremely distorted spiral arms or long tidal tails, indicating a major interaction.' 81 galaxies;

(iii) possibly visually asymmetric: 'Possible/mild asymmetry. For example, a galaxy might be slightly 'bent', indicating some interaction with a passing galaxy or might show evidence of a very minor merger.' 19 galaxies;

(iv) uncertain: 'Galaxies that are small or unclear enough that a reliable classification is impossible.' 15 galaxies.

Fig. 9 shows examples of galaxies in the normal, definitely visually asymmetric and uncertain categories. The features included in the 'definitely visually asymmetric' category were: tidal tails, warps and evidence of double cores or in-progress mergers. Importantly, we were not simply identifying major mergers, but rather a range of visual asymmetries. If there was at least 66 per cent agreement that a galaxy was 'definitely visually asymmetric', it was placed in the visually asymmetric sample used throughout this work. Individual classification results are given in the appendix to this paper.

We note the similarity of our method to that used by the Intermediate MAss Galaxy Evolution Sequence (IMAGES) survey (Yang et al. 2008) to classify kinematic maps. However, unlike the IMAGES survey work, we used a qualitative approach to identify visual asymmetry and a quantitative standard for kinematic asymmetry.

We chose to be conservative in excluding galaxies that were only possibly visually asymmetric from the list of visually asymmetric galaxies. This was because we did not want to err on the side of misclassifying normal galaxies as visually asymmetric. For our purposes, it was better to have a cleaner sample of visually asymmetric galaxies, even at the potential cost of losing a small fraction. Similarly, galaxies with apparent near companions, but no visual evidence of asymmetry, were classified as normal.

We find no difference in the errors on the SDSS photometric PAs for galaxies classified as visually asymmetric and normal. Galaxies with offset kinematic and photometric PAs were generally visually classified as asymmetric. The relationship between offset between kinematic and photometric PAs and kinematic asymmetry will be the subject of future work by the SAMI Galaxy Survey team (Bloom et al., in preparation; Bryant et al., in preparation). An offset between the kinematic and photometric PA would likely qualify a galaxy as 'asymmetric' for the purposes of this work.

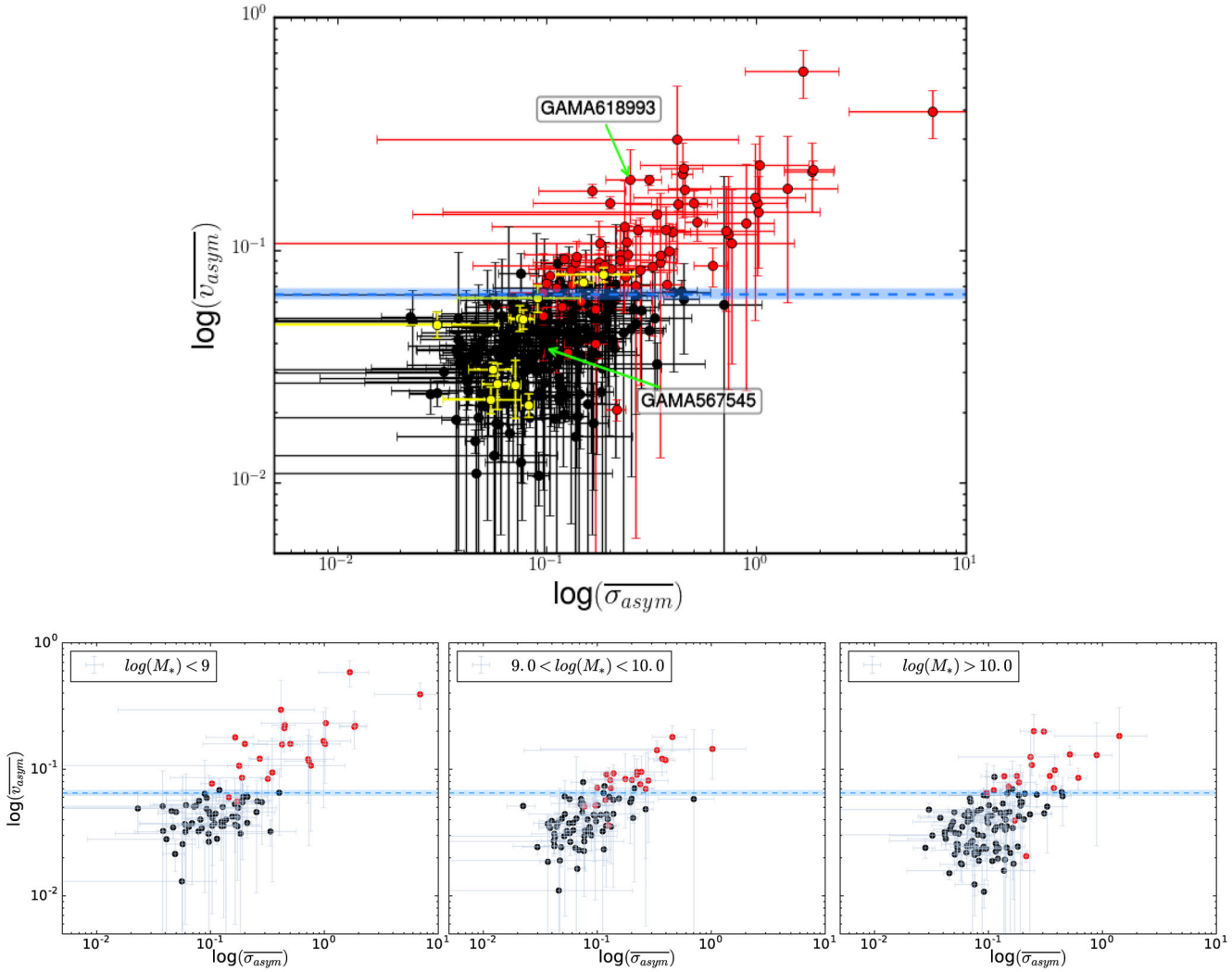

Figure 8. These plots summarize the results of kinemetry for the 360 galaxies in our sample (top) and three stellar mass bins (bottom row). The median kinemetric asymmetries for both velocity and velocity dispersion across fitted ellipse radii are normalized over the rotational velocity and plotted against each other. The sample was visually classified morphologically (using the SDSS DR10 images), with visually asymmetric galaxies shown here in red and 'possibly asymmetric' galaxies in yellow. We show the $\overline{v_{\rm asym}}$ cutoff for kinematic asymmetry derived in the text (blue, dashed line). The two example galaxies from Fig. 6, GAMA567545 (the normal galaxy) and GAMA618993 (the asymmetric galaxy) are indicated by the green arrows, for reference.

4 DISTINGUISHING BETWEEN KINEMATICALLY NORMAL AND ASYMMETRIC GALAXIES IN THE SAMI GALAXY SURVEY

Fig. 10 shows histograms of the distributions of median velocity and velocity dispersion asymmetries, $\overline{v_{\rm asym}}$ and $\overline{\sigma_{\rm asym}}$. The complete sample is shown in grey. The distribution in both cases is smooth and peaked at low values, with a tail. It is not immediately obvious where to place a cutoff for galaxies to be classified as kinematically asymmetric or normal.

Fig. 10 also shows galaxies visually identified as asymmetric in red and normal galaxies in black. Visually asymmetric galaxies tend to have higher $\overline{v_{\rm asym}}$ and $\overline{\sigma_{\rm asym}}$, which provides a reasonable basis for the cutoff.

The good agreement between the visual classification and measured kinematic asymmetry suggests that if there is kinematic disturbance, the image will almost always show a signature of that disturbance. While kinematics provide a more physical measure of disturbance, the images show the effects of that disturbance. Galaxies 'incorrectly' visually classified cannot be quantitatively distinguished, due the qualitative nature of the visual classification.

Fig. 11 shows the fractional completeness and contamination from 0 to 1.0 of the samples of visually asymmetric and normal galaxies across a range of values on either side of the crossover points of the visual classification histograms in Fig. 10, for $\overline{v_{\rm asym}}$. Ideally, we would like to maximize completeness (which we define as fraction of galaxies with the same kinematic classifications as visual) and minimize contamination (defined as fraction in each kinematic bin with opposite visual classifications) for both visually normal and asymmetric galaxies. The distance between the intersection points of the curves for visually normal and asymmetric galaxies indicates how viable it is to choose a single kinematic cut-off point for that purpose. We found that the distance between intersection points was much greater for $\overline{\sigma_{\rm asym}}$ than for $\overline{v_{\rm asym}}$ (0.032 against 0.013). This means that it is significantly harder to choose a cutoff based on $\overline{\sigma_{\rm asym}}$ that will give both high completeness and low contamination for both normal and asymmetric galaxy populations.

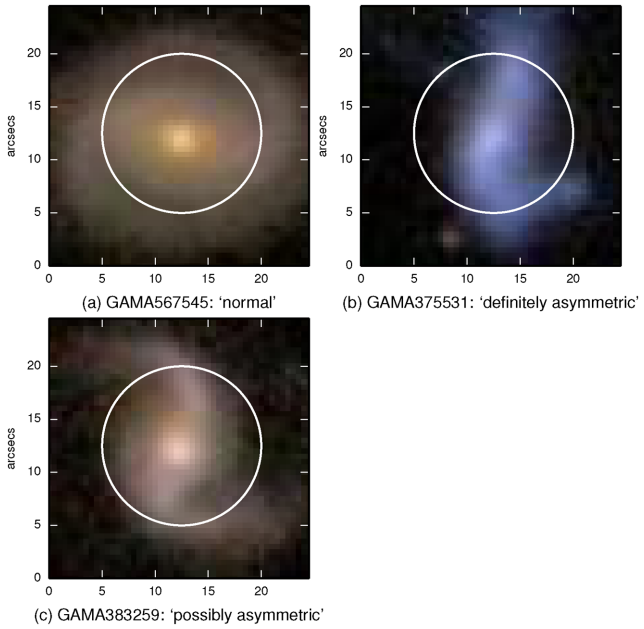

Figure 9. From top left, we give: examples of 'normal', 'definitely visually asymmetric' and 'possibly visually asymmetric' galaxies from the morphological classification. The SAMI instrument field of view is shown as a white circle. Images are from the SDSS DR10 catalogue used to classify the galaxies.

This is the case whether we try a cut based on $\overline{\sigma_{\rm asym}}$ or a combination with $\overline{v_{\rm asym}}$.

Accordingly, we cut by median velocity asymmetry, $\overline{v_{\rm asym}}$. The intersection points of the curves representing contamination and completeness are 0.071 and 0.058, respectively. We, thus, choose the mid-point of these values, giving a cut-off value of $\overline{v_{\rm asym}} > 0.065$ for a galaxy to be considered asymmetric (shown in blue in Fig. 10). This yields a contamination of 3 per cent and completeness of 90 per cent for visually asymmetric galaxies and contamination of 10 per cent and completeness of 95 per cent for visually normal galaxies. Of course, the by-eye classification we take as our guide is imperfect and qualitative, so there is some uncertainty in these measures. Nevertheless, the degree to which it is possible to map the visual classification on to the kinemetric one does point to an underlying physical similarity between the features selected for by each.

The red points in Fig. 8 are galaxies classified as visually asymmetric and the black points are visually normal galaxies. The larger scatter between the visually asymmetric and normal galaxies in $\overline{\sigma_{\rm asym}}$ shows again that more visually asymmetric galaxies would be misclassified as asymmetric by applying a cutoff in both $\overline{v_{\rm asym}}$ and $\overline{\sigma_{\rm asym}}$. We note that the SINS survey team also used the mean of the higher order mode values, whereas we took the median. We found that taking the mean increased the contamination between the distributions of visually asymmetric and normal galaxies. A similar analysis to that performed above yielded a crossover contamination of 8 per cent for visually asymmetric galaxies.

We also show galaxies classified as visually 'possibly visually asymmetric' in yellow in Fig. 8. We note that these galaxies are almost all (90 per cent) in the lower section or 'normal area' of the plot, with only two galaxies falling above our $\overline{v_{\rm asym}} > 0.065$ line. This supports our decision to exclude them from the sample of visually asymmetry galaxies.

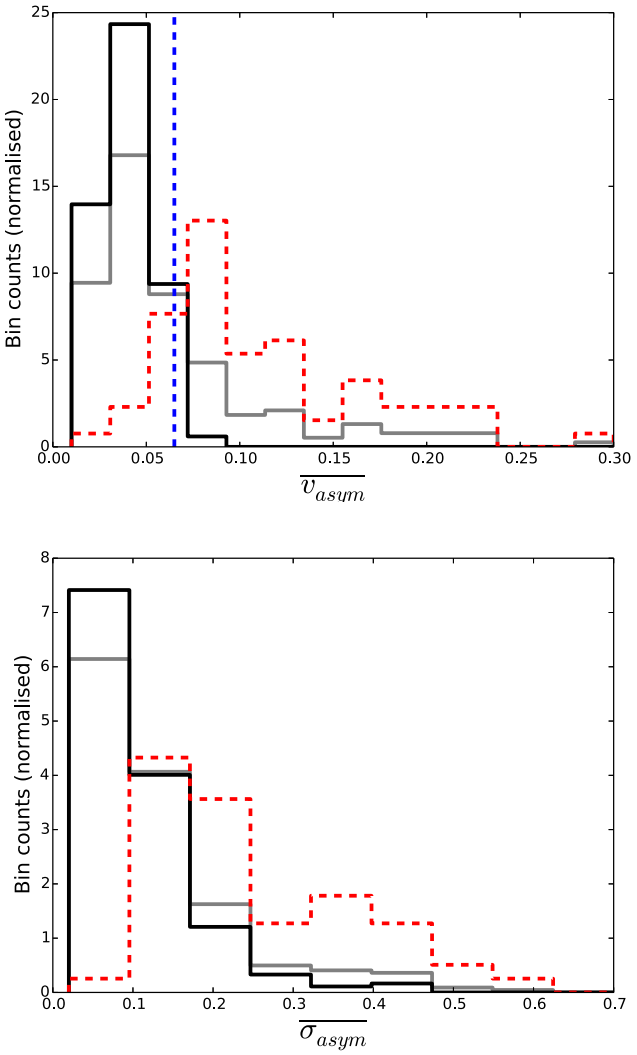

Figure 10. We show normalized histograms of $\overline{v_{\rm asym}}$ (top panel) and $\overline{\sigma_{\rm asym}}$ (bottom panel) for the whole sample (grey), visually classified normal (black) and asymmetric (red, dashed) galaxies. The cut-off value, $\overline{v_{\rm asym}} = 0.065$, is shown in blue.

Galaxies classified as visually normal but kinematically asymmetric are clustered around the boundary value of $\overline{v_{\rm asym}} \sim 0.065$. The qualitative visual classification does not allow us to further distinguish these galaxies. The advantage of kinemetry is that it removes this qualitative component. Of the galaxies classified as morphologically perturbed but kinematically normal, some have images which appear to include foreground objects, which may contribute to the 'misclassification'.

We note that galaxies in the sample have different effective radii, so are covered to different extents by the SAMI instrument field of view. We do not, however, find that coverage influences the outcome of fits by kinemetry, so we disregard this as a possible bias in our results.

Using our kinemetry results and cutting the sample at $\overline{v_{\rm asym}} > 0.065$, we calculate a kinematic asymmetric fraction of 23 per cent $\pm$ 7 per cent. This is comparable to the complex kinematics fraction of 26 per cent $\pm$ 7 calculated by the IMAGES survey (Yang et al. 2008) for galaxies with $z \sim 1$, using a visual classification method similar to ours described in Section 3.3.

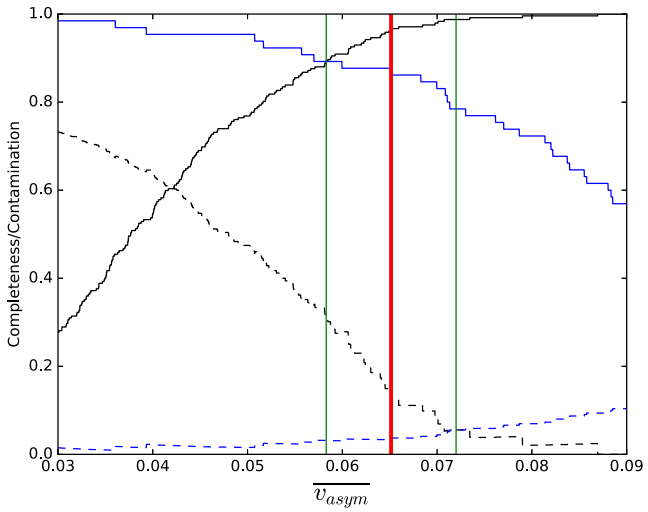

Figure 11. These curves show contamination (dashed) and completeness solid for visually asymmetric (blue) and visually normal (black) galaxies, at a range of values of $\overline{v_{\rm asym}}$. We choose our cut-off point (shown in red) as the mid-point between the points of intersection of the curves for contamination (number of visually normal galaxies classified as kinematically asymmetric and vice versa) and completeness (number of visually asymmetric galaxies classified as kinematically asymmetric, similarly for visually normal galaxies) (shown in green). The points of intersection for contamination and completeness are 0.071 and 0.058, respectively, so we choose a cut-off value of $\overline{v_{\rm asym}} = 0.065$. See Section 4 for a complete explanation.

4.1 Comparison of the kinemetry technique with quantitative morphology

Given that major mergers are known to cause kinematic asymmetry (Shapiro et al. 2008), we determine whether quantitatively morphologically asymmetric galaxies are kinematically asymmetric and whether kinematically asymmetric galaxies are quantitatively morphologically distinct from kinematically normal galaxies. Quantitative morphology techniques such as the Gini (Gini 1912) and M_{20} (Lotz et al. 2004) coefficients and the Concentration/Asymmetry/Smoothness (CAS) categorisation method (Conselice 2003) have been used in previous studies to identify major mergers, as has kinemetry (Shapiro et al. 2008), providing a useful basis for comparison. Simons et al. (2015) compare $\frac{\sigma}{V}$ and quantitative morphology, concluding that kinematically disturbed galaxies, falling off the Tully–Fisher line, also tend to be asymmetric by the standards of quantitative morphology.

To perform this analysis, we use the *r*-band SDSS DR10 images (Ahn et al. 2014). We follow methods in Lotz et al. (2004) and Conselice (2003). To determine the centre of the images used in this analysis, we replicate the method described in Section 3 on the *r*-band SDSS DR10 images for each galaxy.

In this work, errors on G, M_{20} and the CAS Asymmetry coefficient are found by bootstrapping the calculations of the coefficient for each galaxy, adding random noise to the data and calculating the uncertainties from the distribution of these iterations.

4.1.1 The Gini coefficient

The Gini coefficient, G, was developed by economists (Gini 1912) as a descriptor of the distribution of resources amongst a population. $G = 1$ indicates that the entire wealth of a population is concentrated with one individual, whereas $G = 0$ signifies complete equality. It was first used in an astronomical context by Abraham, Van Den Bergh & Nair (2003). Applied to galaxy flux, G becomes a measure of concentration of light, similar to C in the CAS system (see Section 4.1.3). In high-G galaxies, the light is locally concentrated (for instance, there could be a highly dominant bulge). A low-G galaxy would have a smooth, uniform light distribution, without a significant bulge. Alternatively, it could be composed of many small clumps, including regions of star formation that would 'balance out' a central bulge.

G is mathematically defined as (Glasser 1962):

$$G = \frac{1}{\overline{X}n(n-1)} \sum_{i}^{n} (2i - n - 1)X_i, \tag{8}$$

where $\overline{X}$ is (in this case) the mean of the galaxy flux in n total pixels, with X_i being the flux in the ith pixel.

Previous work has used G in combination with M_{20} (Lotz et al. 2004, see Section 4.1.2) and CAS (Conselice 2003, see Section 4.1.3) to identify major mergers.

4.1.2 The M_{20} *coefficient*

The M_{20} coefficient is similar to G, in that it measures the concentration of the spatial distribution of light within a galaxy, but can be used to distinguish galaxies with different Hubble types (Lotz et al. 2004). The total second-order moment of galaxy flux, $M_{\rm tot}$, is defined as the flux f_i in each pixel, multiplied by the squared distance between pixel i and the centre of the galaxy $(x_{\rm c}, y_{\rm c})$, summed over all galaxy pixels:

$$M_{\rm tot} = \sum_{i}^{n} M_i = \sum_{i}^{n} f_i[(x_i - x_{\rm c})^2 + (y_i - y_{\rm c})^2]. \tag{9}$$

M_{20} is then defined as the normalized second-order moment of the brightest 20 per cent of the galaxy's flux. The galaxy pixels are rank-ordered by flux and then M_i (the second-order moment of light for each pixel i) is summed over the brightest pixels until the sum of the brightest pixels is equal to 20 per cent of the total flux:

$$M_{20} = \log_{10}\left(\frac{\sum_i M_i}{M_{\rm tot}}\right) \tag{10}$$

for $\sum i f_i < 0.2 f_{\rm tot}$, where $f_{\rm tot}$ is the total flux, $\sum_i^n f_i$.

4.1.3 CAS asymmetry

The CAS system was developed as a means to distinguish galaxies in different stages of evolution, based on where they fall within a volume derived from the CAS structural parameters (Conselice 2003). The C and A parameters were first developed by Abraham et al. (1996). We will discuss only the application of Asymmetry, henceforth A, as C and S are not intended to describe asymmetries.

To find A, a galaxy image is rotated 180° around its central point and the result is subtracted from the original image. A is then computed as the sum of the absolute values of the residuals, normalized over the sum of the flux in the original image. A is clearly sensitive to any feature that is not rotationally symmetric. These may include spiral arms, areas of intense star formation and merger signatures (Conselice 2003).

It is important to note that A was specifically developed to identify the middle stage of major mergers, in which case the visual asymmetric features resulting from the merger would far outweigh those from ordinary morphology, such as spiral arms. However, in the case of more minor asymmetries, other morphological features

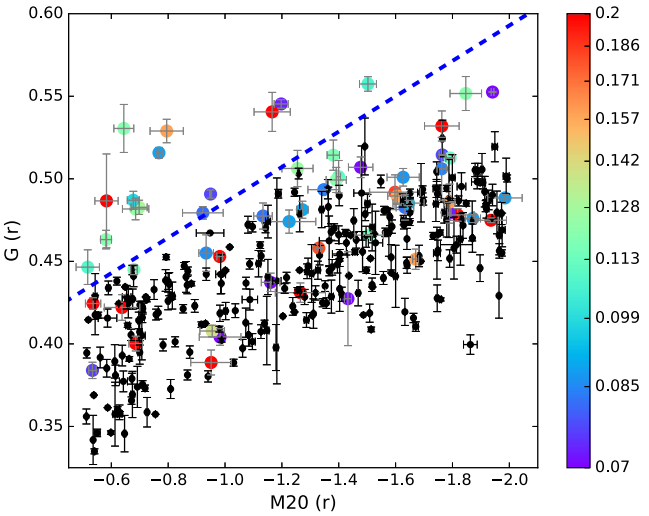

Figure 12. We show M_{20} against G, with kinematic classifications (normal galaxies in black, kinematically asymmetric galaxies in colour). We see that even though the majority of galaxies falling above the line defined in Lotz et al. (2004) are kinematically asymmetric, there are many that would not be identified using this system. The colour bar shows the $\overline{v_{\rm asym}}$ values on a log scale for the kinematically asymmetric points. We see that many of the most kinematically asymmetric points fall below the line.

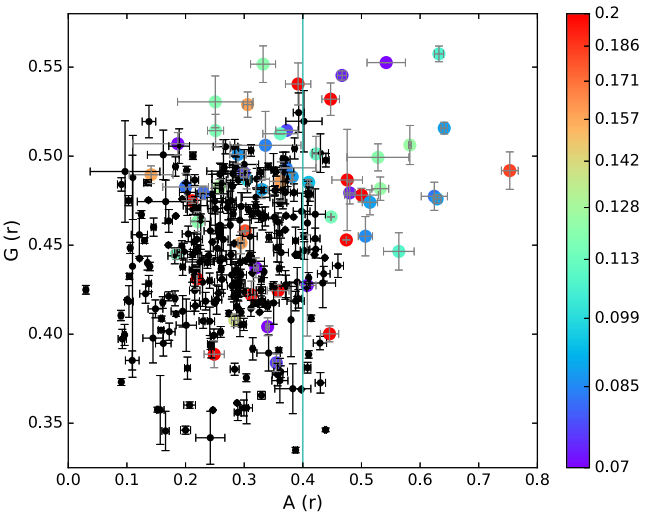

Figure 13. We show the A–G plane for kinematically normal (black) and kinematically asymmetric (coloured) galaxies. Errors are 1σ errors on both axes. As anticipated, only a weak relation emerges between asymmetry and plane location. The blue line indicates $A \sim 0.4$, below which the relationship between A and asymmetry becomes significantly weaker.

may dominate. For example, a relatively small and dim tidal tail would be overshadowed by the presence of bright spiral arms.

4.1.4 Comparison of classifications using kinematics and quantitative morphology

Following previous work (Lotz et al. 2004), Fig. 12 shows M_{20} against G for the galaxies in our sample. The kinematically asymmetric galaxies (coloured) are those with $\overline{v_{\rm asym}} > 0.065$. Lotz et al. (2004) drew a line on the plane to distinguish Ultra-Luminous Infrared Galaxies (ULIRGs) from 'normal' galaxies, shown in Fig. 12 in dashed blue. Whilst all of the galaxies above the line in our sample are kinematically asymmetric, there are also many kinematically asymmetric galaxies which would not be identified using this method. Quantitatively, 79 per cent ± 3 per cent of kinemetrically asymmetric galaxies would be classified as normal by this method. Further, many of the most kinematically asymmetric galaxies, indicated by the colour bar, fall below the line. This is because G and M_{20} measure the spread of light. A galaxy with multiple, bright clumps has a different light distribution profile from a normal galaxy (with one bright, central bulge), but a galaxy with a strong kinematic twist may not, as the ratio of light in the bulge and body of the galaxy may be the same, regardless of the twist.

In Fig. 13, following Conselice, Rajgor & Myers (2008), we show G against A. As in Fig. 12, coloured points are those with $\overline{v_{\rm asym}} > 0.065$. We once again see only a weak relationship between kinematic asymmetry and placement on the plane. Galaxies with $A > 0.4$ are mostly kinematically asymmetric, but below this threshold, there is no significant relation. Indeed, 59 per cent ± 4 per cent of kinematically asymmetric galaxies in our sample lie below $A = 0.4$. As in Fig. 12, some of the most kinematically asymmetric galaxies are not classified as morphologically disturbed using this method. This is because the relationship between A and photometric (also, by extension, kinematic) asymmetry becomes significantly weaker below $A = 0.4$ (Conselice 2003; Conselice et al. 2008). Whilst galaxies with $A > 0.4$ are very likely to be disturbed, below this threshold, normal morphological features (particularly spiral arms) dominate, so true asymmetries are lost. Given that most of our kinematically asymmetric galaxies fall below this threshold, our result is not unexpected.

We conclude that almost all quantitatively morphologically asymmetric galaxies are kinematically asymmetric. Further, kinematics can identify asymmetry in galaxies that appear normal when using these quantitative morphology methods.

5 COMPARISON OF OUR RESULTS WITH HIGH-REDSHIFT STUDIES

Although our method is based on that used by the SINS Survey team, there are some differences. For example, they used the mean of radially calculated kinematic asymmetry values, whereas we used the median and they included the even modes of the velocity fields and odd modes of velocity dispersion fields in the calculation of velocity and velocity dispersion asymmetry. In order to more directly compare our results with the SINS Survey results, we recalculated our kinematic asymmetry values, applying their method. Fig. 14 shows our results (black points), along with a sample of those from the SINS Survey, including artificially redshifted local spiral galaxies from the SINGS Survey (turquoise triangles), artificially redshifted local ULIRGS (yellow triangles) and galaxies observed by the SINS Survey team at high redshift (purple points) (Shapiro et al. 2008). We also show a sample of high redshift ($2.0 < z < 2.7$) sub-millimetre galaxies (SMGs) from Alaghband-Zadeh et al. (2012) (red crosses). Of the SMGs, those which are AGN candidates are also noted (red diamonds superimposed on the red crosses). We see that the spread of our values does not change significantly, despite the recalculation.

Applying their version of kinemetry to the SINS Survey sample led to an estimated major merger fraction of ∼25 per cent (Shapiro et al. 2008). Due to the high redshift of their sample ($z \sim 2$), which led to correspondingly low H α S/N in their data, even their normally classified galaxies have higher kinematic asymmetry values than the majority of the galaxies in our sample (see Fig. 14). Gonçalves et al. (2010) have argued that, in fact, degrading the resolution of data (as

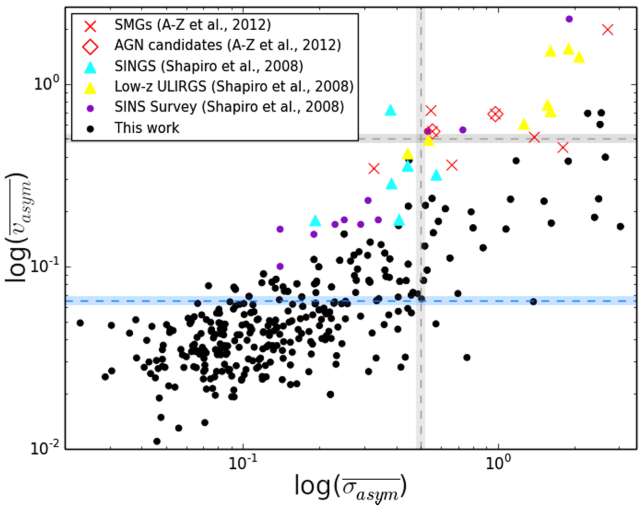

Figure 14. This figure shows the mean velocity and velocity dispersion asymmetries for galaxies in our sample and those from several other works using kinemetry (as in legend). Error bars have been removed for clarity. The grey lines indicate the kinematic asymmetry cutoffs from the SINS Survey work (Shapiro et al. 2008) and the blue line is the cutoff we developed for use on our data.

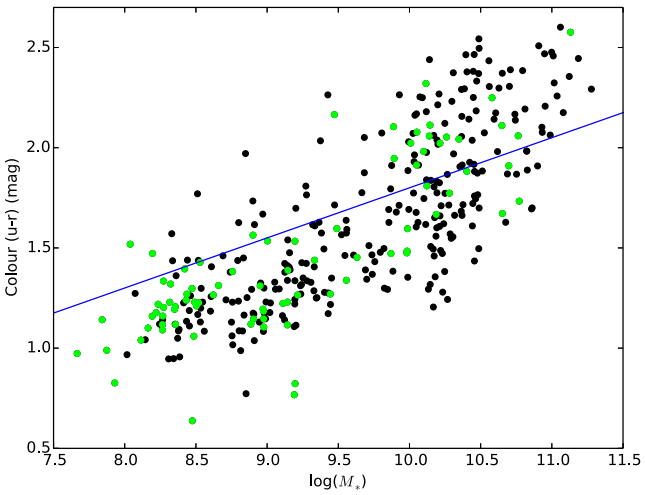

Figure 15. This plot gives colour and stellar mass for the sample used in this work of kinematically identified normal (black) and kinematically asymmetric galaxies (green). The dark blue line separates the blue cloud and red sequence and is taken from Schawinski et al. (2014). The data used were taken from the GAMA Data Release 2 catalogues StellarMasses and ApMatchedPhotom (Hill et al. 2011; Taylor et al. 2011).

a proxy for higher redshift) leads to decreased kinematic asymmetry values, rather than the increased values found by the SINS Survey. However, it is not clear how a corresponding increase in noise for high-redshift data will affect the results. This is a still open question and, accordingly, our result of a kinematic asymmetric fraction of 23 per cent ± 7 per cent should not be directly compared with the result in Shapiro et al. (2008). The SINS Survey also required their galaxies to have continuum S/N ≥ 3 that may have biased their sample towards galaxies with high SFR, influencing the distribution of kinematic asymmetries.

All high-redshift samples in Fig. 14 (both observed and artificially redshifted) fall entirely above our cutoff for kinematic asymmetry, with the exception of two redshifted SINGS spiral galaxy. Given the results from the SINS Survey that showed how decreased S/N (either artificially or from increased redshift) can increase kinemetric coefficients, this is not surprising. Nevertheless, the higher kinemetric coefficients may also be reflective of intrinsic kinematic asymmetry.

If we were to naively apply the cutoff from the SINS Survey work (mean velocity and velocity dispersion asymmetry = 0.5), we would have a major merger rate of 1 ± 4 per cent. There have been a number of other local merger rates, including those calculated using simply close pairs (e.g. De Propris et al. 2014), quantitative morphology (e.g. Lotz et al. 2008, 2011) and a combination of the two methods (Casteels et al. 2014). These local major merger rates range from ∼1–4 per cent and so are broadly consistent with the value from this work combined with the SINS Survey cutoff. However, given the difference in redshift between the SINS Survey and SAMI Galaxy Survey, this should not be interpreted as necessarily signifying scientific agreement. At $z \sim 1$, Stott et al. (2014) use kinemetry (approximately following the Shapiro et al. 2008) method, using a cutoff of $K_{\rm tot} > 0.5$) to derive a major merger rate of 10 per cent.

We further note that of the SAMI Galaxy Survey sample galaxies which fall above the SINS Survey cut-off, 66 per cent fall above the major merger lines in Figs 12 and 13.

6 THE RELATIONSHIP BETWEEN KINEMATIC ASYMMETRY, COLOUR AND STELLAR MASS

Colour is directly linked to star formation history. We investigate whether processes causing kinematic asymmetry influence star formation history, as revealed by a change in colour. Several studies have established links between colour and kinematic abnormality, e.g. Conselice, Bershady & Gallagher (2000), Kannappan, Fabricant & Franx (2002) and Neichel et al. (2008), finding that asymmetric galaxies are bluer than their normal counterparts. We here determine the position of our sample of kinematically asymmetric galaxies on the colour–stellar mass plane. Fig. 15 shows the $u - r$ rest-frame colour–stellar mass distribution for normal (black) and kinematically asymmetric (green) galaxies. We used a cut from Schawinski et al. (2014) (dark blue in Fig. 15) to separate the blue cloud and red sequence. We see that 75 ± 10 per cent of kinematically asymmetric galaxies fall in the blue cloud and only 25 ± 11 per cent fall on the red sequence. For comparison, 65 ± 7 per cent of normal galaxies are in the blue cloud and 34 ± 8 per cent of normal galaxies are in the red sequence.

Fig. 16 shows an inverse relationship between stellar mass and kinematic asymmetry and a Spearman rank correlation test for $\overline{v_{\rm asym}}$ and stellar mass gives $\rho = -0.30$, p-value $= 8.40 \times 10^{-9}$. We further show the fraction of kinematically asymmetric galaxies in bins of stellar mass that also dramatically declines with increasing stellar mass. Given that colour and stellar mass are strongly correlated, the apparent tendency of kinematically asymmetric galaxies to be bluer, compared to their normal counterparts, is not surprising.

To test whether $\overline{v_{\rm asym}}$ and colour are related independently of mass, we performed a series of partial Pearson correlation tests between $\overline{v_{\rm asym}}$ and colour (accounting for the correlation of colour with stellar mass) on the individual branches and the whole sample. The results of the correlation test between colour and $\overline{v_{\rm asym}}$ for the red and blue branches were $\rho = 0.054$, p-value $= 0.57$ and $\rho = 0.096$, p-value $= 0.13$, respectively. For the whole sample, the result was $\rho = 0.11$, p-value $= 0.028$. This indicates that there is at best

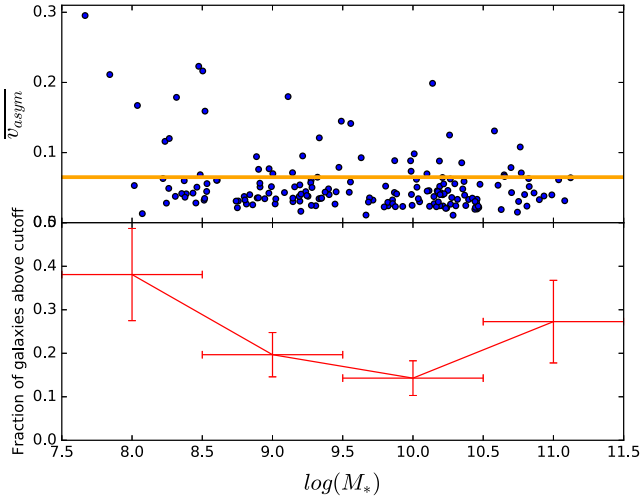

Figure 16. $\overline{v_{\rm asym}}$ is plotted against against stellar mass for the galaxies in our sample. The orange line shows our kinematic asymmetry cutoff, such that all galaxies above it are considered asymmetric. The bottom panel shows the fraction of galaxies, in bins of stellar mass (shown as horizontal error bars), above the asymmetry cutoff. This fraction decreases as a function of stellar mass.

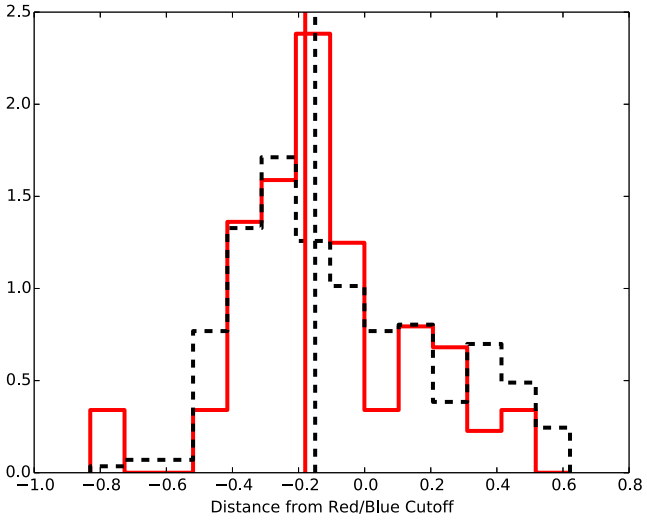

Figure 17. We show a normalized histogram of distance (in colour space) from red/blue cutoff for kinematically asymmetric (red) and normal (black, dashed) galaxies. The median offset for each distribution is shown by the vertical lines. There is no significant offset between the kinematically asymmetric and normal medians, indicating that, independent of mass, there is no relationship between colour and $\overline{v_{\rm asym}}$.

marginal correlation between colour and kinematic asymmetry, either in the separate branches or the full sample.

The small positive correlation between $\overline{v_{\rm asym}}$ and colour over the full sample is explained by a slight deficit of high mass, blue branch kinematically asymmetric galaxies in Fig. 15. Examining the proportion of kinematically asymmetric galaxies in each branch above $\log(M_*) > 10.0$, 15 of 86 (17 ± 3 per cent) of red galaxies are kinematically asymmetric, compared to 7 of 66 (10 ± 3 per cent) of blue galaxies. Although the difference is marginally significant, a possible physical explanation for this comparative deficit of high-mass, blue branch kinematically asymmetric galaxies may be related to the lower gas fraction in red galaxies. Incoming gas from an interaction is likely to settle to rotate with the main galaxy mass in a high-gas fraction (blue) galaxy. However, in a low-gas fraction, red galaxy, it may be easier to preserve any difference in angle of rotation between newly accreted gas and the main disc. Given that, for kinemetry, we fit the PA of the disc from *r*-band photometry that traces the stellar component, any offset in the PA of the gas would register in the higher order moments (Bryant et al., in preparation).

Fig. 17 shows a histogram of the distance of each galaxy from the red/blue cutoff in Fig. 15, in terms of colour as well as the medians of the distributions. A negative distance indicates that the galaxy is in the blue branch, whereas red galaxies have positive distances. A negative shift in the median distance would indicate that kinematically asymmetric galaxies are bluer than normal galaxies, independent of the negative correlation between mass and $\overline{v_{\rm asym}}$. The medians are -0.14 ± 0.014 (normal galaxies) and -0.18 ± 0.027 (kinematically asymmetric galaxies). There is an offset of 0.03 ± 0.03, which is not significant. From this result, we conclude that the dominant relationship is between $\overline{v_{\rm asym}}$ and stellar mass.

6.1 Explaining the inverse correlation between stellar mass and $\overline{v_{\rm asym}}$

There are several possible reasons for the strong observed relationship between mass and kinematic asymmetry. We rule out that the increased $\overline{v_{\rm asym}}$ is a result of poorer S/N in the low-mass objects, as there is no significant trend between the Hα S/N and galaxy mass. Further, there is no statistical relationship between the number of effective radii covered in the analysis and kinematic asymmetry, which excludes any boost in $\overline{v_{\rm asym}}$ in low-mass galaxies purely due to their size. This is because the low-mass galaxies in the SAMI Galaxy Survey sample are at lower redshift and have proportionately more Hα gas (Allen et al. 2015).

The Tully–Fisher relation (Tully & Fisher 1977) links the rotational velocity of galaxies to their absolute magnitude, which is, in turn, proportional to stellar mass. The dwarf galaxies in our sample have lower rotational velocities than high-mass galaxies. Given that, in this work, higher order kinemetry terms are normalized relative to the first-order velocity field, it is plausible that kinematic asymmetries of the same intrinsic amplitude would yield greater kinemetric signatures in low-mass galaxies, as low-mass galaxies have disproportionately low velocities. Low-mass galaxies have also previously been found to have complex kinematics by a variety of metrics (e.g. van Zee, Skillman & Salzer 1998; Cannon et al. 2004; Lelli, Verheijen & Fraternali 2014). Further, alternative measures of kinematic asymmetry, such as that in the rotation curve (Barton et al. 2001; Garrido et al. 2005), have found dwarf galaxies to have both high kinematic asymmetry and low rotational support. It has additionally been long established that low-mass galaxies have irregular morphologies (Roberts & Haynes 1994; Mahajan et al. 2015; Simons et al. 2015) that may be linked to their irregular kinematics.

Escala & Larson (2008) link the stochastic formation of massive instabilities to rotational velocity. They find that the mass of gaseous instabilities is inversely proportional to angular rotational velocity:

$$M_{\rm cl}^{\rm max} = \frac{\pi^4 G^2 \Sigma_{\rm gas}^3}{4\Omega^4}, \tag{11}$$

where $M_{\rm cl}^{\rm max}$ is the maximum mass of unstable regions, Σ is the gas surface density and Ω is the angular rotation speed, $\frac{V_c(R)}{R}$, of the disc. Given that, in order to meet the condition for rotational support inside a given radius R,

$$\Omega^2 = \frac{\pi G \Sigma_{\rm gas}}{\nu R}, \tag{12}$$

where $\nu = M_{\rm gas}/M_{\rm tot}$, the maximum instability mass can be expressed as a function of gas fraction:

$$M_{\rm cl}^{\rm max} = \frac{\pi^2 \nu^2 R^2 \Sigma_{\rm gas}}{4}. \quad (13)$$

Given their typically high gas fractions (Geha et al. 2006; Huang et al. 2012), i.e. high ν, low-mass galaxies are likely to have comparatively large maximal sizes of these instabilities. Assuming that large instabilities leave kinematic signatures corresponding to increased kinemetric coefficients, this effect may contribute to the trend observed here. This theory is supported by work such as Amorín et al. (2012), in which complex Hα kinematics in dwarf galaxies are linked to the presence of multiple star-forming clumps. Further, Green et al. (2014) find that for star-forming galaxies, high gas fraction (inferred from SFR density) is linked to high $\frac{\sigma_{\rm m}}{V}$, where $\sigma_{\rm m}$ is the mean velocity dispersion and V is the circular velocity. This measure can be used as a proxy for turbulent support, relative to rotational support. An excess in turbulent support may contribute to the higher kinematic asymmetry in low-mass, high-gas fraction galaxies in our sample. Simons et al. (2015) find that below $\log(M_*) \sim 9.5$, there is increased scatter off the Tully–Fisher relation to lower velocity, due to low-mass galaxies having high $\frac{\sigma_{\rm m}}{V}$. This scatter e.g. (Kannappan et al. 2002; Cortese et al. 2014) would amplify the effect of low rotation on the normalization of higher order kinemetry terms. We note that kinemetry and $\frac{\sigma_{\rm m}}{V}$ probe kinematic disturbance on different scales. Whereas kinemetry is used to identify features dominating the optical galaxy that are larger than a resolution element, $\frac{\sigma_{\rm m}}{V}$ measures turbulence on scales of less than a pixel. Further exploration of the relationships between $\overline{v_{\rm asym}}$, $\frac{\sigma_{\rm m}}{V}$ and stellar mass will be the subject of future work.

It is also possible that the observed relationship is due to environmental effects. For example, dwarf galaxies are more likely to be satellites of high-mass galaxies, which would perturb their kinematics. They are also more likely to undergo interactions with more massive partner galaxies, which would cause them to experience greater kinematic perturbation than a higher mass galaxy under the same circumstances. In contrast, however, Kirby et al. (2014) find that the disturbance in the kinematics of isolated and satellite low-mass galaxies are similar. The degree to which environment influences kinematic asymmetry will be the subject of future study.

7 STAR FORMATION IN KINEMATICALLY ASYMMETRIC GALAXIES

Several processes known to cause kinematic asymmetry have also been suggested to influence star formation, such as major mergers (Ellison et al. 2013), minor mergers (Kaviraj et al. 2009; Kaviraj 2014) and tidal interactions (Bekki & Couch 2011). We here quantitatively determine this relationship by comparing different measures of SFR and distribution of star formation.

7.1 Comparison of SAMI Galaxy Survey, SDSS and GAMA SFRs

The SAMI Galaxy Survey SFRs, derived from the Hα flux, were calculated from annular Voronoi binned data cubes (in annular Voronoi binning, the adaptive bins are constrained to an annulus of a specific radius; see Schaefer et al. 2017). These cubes were binned to a target continuum emission S/N of 10 in a 200 Å-wide window around the wavelength of H β. The S/N calculation includes covariance between spaxels when calculating the variance. Each binned spectrum is then fit by LZIFU (Ho et al., 2016). The Hα flux is then dust-corrected in each bin, using the Calzetti (2001) dust correction, which models the dust as a foreground screen. The Hα fluxes in each bin were converted to luminosities and from that to SFRs using the Kennicutt (1998) relation assuming a Salpeter (Salpeter 1955) initial mass function. For a complete description of the SAMI Galaxy Survey SFRs, see Schaefer et al. (2017), from which the data used here were taken.

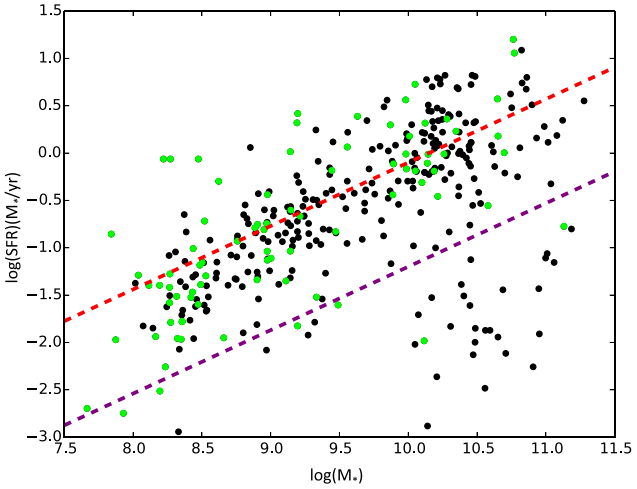

Figure 18. This figure shows SFR and stellar mass for normal galaxies (black) and kinematically identified asymmetric galaxies (green). We show the SFR main sequence from Noeske et al. (2007) (red dashed line), and the main-sequence cutoff (purple dashed line). We see that asymmetric galaxies lie almost exclusively above the purple line, whereas normal galaxies are more evenly distributed.

The main sequence of star formation is a relation defined by Noeske et al. (2007) (for $z < 1$) that describes the SFR of typical galaxies, at a given stellar mass. The main sequence is defined as:

$$\log({\rm SFR}) = (0.67 \pm 0.08)\log(M_*) - (6.19 \pm 0.78). \quad (14)$$

Fig. 18 shows the SFR–mass plane for our galaxies, using the SAMI Galaxy Survey SFRs, as well as the main sequence of star formation (in red). Kinematically asymmetric galaxies are shown in green and we see that there are few asymmetric galaxies below the main sequence of star formation. This means that almost all kinematically asymmetric galaxies are star-forming, rather than quiescent. The lower bound for galaxies to be considered part of the main sequence (shown in purple in Fig. 18) was derived using the same method as Noeske et al. (2007), i.e. that there should be an equal number of galaxies above and below the line of the main sequence itself. We find a lower bound of:

$$\log({\rm SFR}) = (0.67 \pm 0.08)\log(M_*) - (7.34 \pm 0.78). \quad (15)$$

Examining the SSFRs of kinematically asymmetric galaxies compared to normal galaxies, they are only marginally different (with a two-sample Kolmogorov–Smirnov test giving $p = 0.06$). Fig. 19 shows histograms of the SSFR for kinematically asymmetric and normal galaxies, again using the SAMI Galaxy Survey SFRs. We find that the offset in the medians for the kinematically asymmetric and normal galaxies is not significant, indicating that there is no significant increase in SSFR in kinematically asymmetric galaxies (see Table 2). The error is calculated, here and henceforth, using the median correction to the standard error on the mean (where σ is the standard deviation of the population and N is the population size):

$${\rm error}_{\rm median} = 1.253 \times \frac{\sigma}{\sqrt{N}}. \quad (16)$$

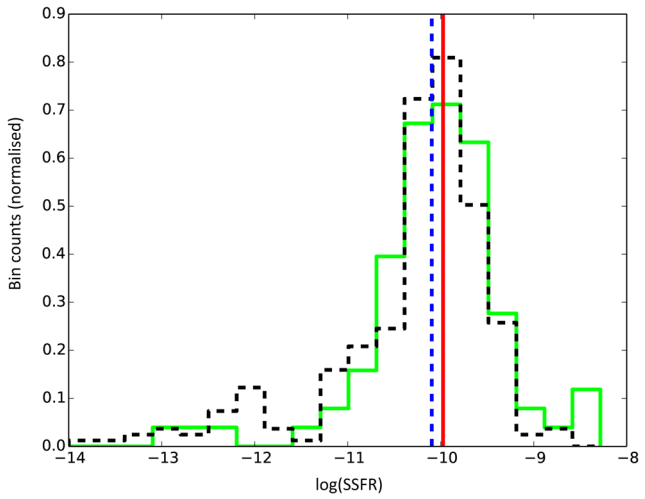

Figure 19. This figure is a histogram of the SSFR for normal (black, dashed) and kinematically asymmetric (green) galaxies in the sample. The medians SSFRs for kinematically asymmetric and normal galaxies are red and blue (dashed), respectively. The offset between the medians is within the error, so is not considered significant.

Table 2. Median log(SSFR) for kinematically asymmetric and normal galaxies (given as $\overline{\log(\mathrm{SSFR})}_p$ and $\overline{\log(\mathrm{SSFR})}_n$, respectively) and offsets between the two when using the SAMI Galaxy Survey, GAMA Survey and SDSS Survey SFRs, respectively. The offsets for the SAMI Galaxy Survey and SDSS values are not significant, due to the overlap in errors on the median SSFRs for asymmetric and normal galaxies.

Data sample	$\overline{\log(\mathrm{SSFR})}_p$	$\overline{\log(\mathrm{SSFR})}_n$	$\overline{\log(\mathrm{SSFR})}$ offset
SAMI Galaxy Survey SFR	-9.97 ± 0.10	-10.10 ± 0.066	0.12 ± 0.12
GAMA Survey SFR	-9.72 ± 0.17	-10.05 ± 0.10	0.33 ± 0.20
SDSS Survey SFR	-10.04 ± 0.12	-10.19 ± 0.070	0.15 ± 0.15

To further analyse the relationship between SFR and kinematic asymmetry, we used two more measurements of SFRs to compare with the SAMI Galaxy Survey values. These were the GAMA Survey SFRs used in 2.4 and SDSS DR7 SFRs,[3] both of which were also obtained from the Hα flux.

The GAMA Survey SFRs were calculated by taking a measurement of the Hα emission at the centre of the galaxy using a 2 arcsec fibre and applying an aperture correction. The correction is calculated based on the proportion of the *r*-band continuum light of the galaxy captured within the size of the fibre, using a method from Hopkins et al. (2003). There is an assumption that the Hα emission scales directly with the *r*-band stellar continuum. A dust correction is applied from the Balmer decrement.

The SDSS DR7 SFRs are constructed using a method based on that in Brinchmann et al. (2004) and a model from Charlot & Longhetti (2001), in which a measurement of Hα emission is taken at the centre of the galaxy and then an aperture correction is applied, but the colour of the galaxy is considered, yielding a more accurate total measurement. They do this by calculating the light outside the fibre and then fit stochastic models, similar to those used in Salim et al. (2007), in which *ugriz* photometry is fit to a variety of dust-attenuated population synthesis models. We note that only ∼250 of our galaxies had corresponding SDSS DR 7 SFRs. However, this reduction in sample size was spread equally across kinematically asymmetric and normal galaxies, so did not introduce bias.

Table 2 shows median SSFRs for kinematically asymmetric and normal galaxies and the offsets between the two. The GAMA Survey SFRs yield a marginally significant offset in the medians, whereas there is no offset from the other two methods. Whilst the GAMA Survey results are still only marginally significant, they do represent a significant difference from the spatially resolved SAMI Galaxy Survey results. This is a result of the different methods of calculating SFR. The GAMA Survey SFRs are predicated on the assumption that the global SFR is directly proportional to the SFR of the region of the galaxy contained within a fibre placed at the centre. This leads to an overemphasis on central SFR. By contrast, the SDSS DR7 SFRs, whilst still measuring SFR within a central fibre, modify their aperture correction by considering the global colour of the galaxy, which is linked to global SFR. Finally, the SAMI Galaxy Survey SFRs are intrinsically global, as they measure SFR in individual spaxels across the galaxy, although there is a small aperture effect outside the SAMI instrument bundle (Richards et al., 2016).

If we calculate the SAMI Galaxy Survey SFR within 2 arcsec (the size of the GAMA Survey fibre measurements) and then apply the GAMA Survey aperture corrections, we find the offset between the SSFRs of kinematically asymmetric and normal galaxies is 0.36 ± 0.14 dex. When comparing the aperture corrected values inside 2 arcsec to the standard SAMI Galaxy Survey values, the median SSFRs for kinematically asymmetric and normal galaxies increase by 0.27 ± 0.12 and 0.04 ± 0.06 dex, respectively. Although the effect is only $\sim 2\sigma$ significant, the GAMA Survey method of extrapolating central SFR throughout the disc appears to lead to an overestimation of extended SFR in some galaxies. The more centrally peaked the SFR, the greater the resulting overestimation. That this effect is strongest for kinematically asymmetric galaxies indicates that SFR in asymmetric galaxies is more centrally concentrated than it is in normal galaxies.

7.2 Kinematic asymmetry and concentration of star formation

Fig. 20 shows $\overline{v_{\mathrm{asym}}}$ against the ratio of Hα half-light radius to *r*-band continuum half-light ($\frac{r_{50,\mathrm{H}\alpha}}{r_{50,\mathrm{cont}}}$), both for all galaxies in our sample (top panel) and for only those galaxies with $\log(M_*) > 10.0$ (bottom panel). The $\frac{r_{50,\mathrm{H}\alpha}}{r_{50,\mathrm{cont}}}$ ratio is calculated from the dust-corrected SAMI Galaxy Survey Hα map and *r*-band continuum map for each galaxy. A curve of growth is calculated for both maps, defining the proportion of emission contained within a given radius. The r_{50} radius is the radius containing 50 per cent of the emission. Consequently, $\frac{r_{50,\mathrm{H}\alpha}}{r_{50,\mathrm{cont}}}$ is an indicator of the scale of star formation in a galaxy, compared to the stellar light (Schaefer et al. 2017).

We see an offset of 0.08 ± 0.03 in the median $\frac{r_{50,\mathrm{H}\alpha}}{r_{50,\mathrm{cont}}}$ for kinematically asymmetric and normal galaxies and a Spearman's rank correlation test shows that there is an inverse correlation between $\overline{v_{\mathrm{asym}}}$ and $\frac{r_{50,\mathrm{H}\alpha}}{r_{50,\mathrm{cont}}}$, with $\rho = -0.19$ and p-value $= 7.6 \times 10^{-4}$, meaning that kinematically asymmetric galaxies have increased concentration of Hα emission, compared to normal galaxies, and thus have increased central star formation.

It is possible that stochastic bursts of star formation in low mass galaxies may lead to more scatter in $\frac{r_{50,\mathrm{H}\alpha}}{r_{50,\mathrm{cont}}}$. If we restrict our sample

[3] SDSS DR7 SFRs are taken from 'gal_totsfr_dr7_v5_2.fits.gz', obtained at http://www.mpa-garching.mpg.de/SDSS/DR7/sfrs.html

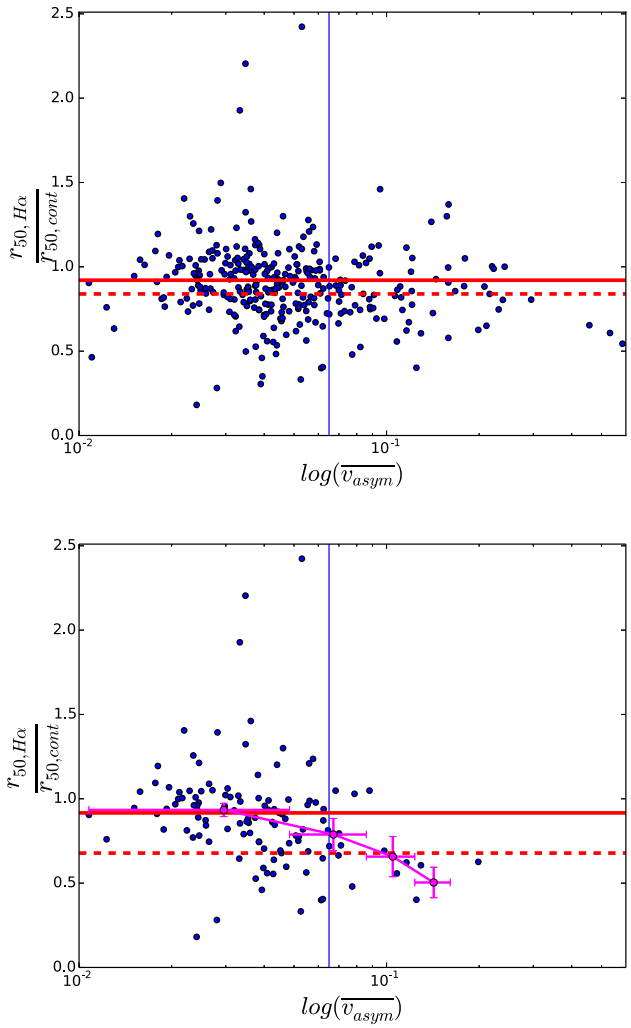

Figure 20. We show $\log(\overline{v_{\rm asym}})$ against $\frac{r_{50,{\rm H}\alpha}}{r_{50,{\rm cont}}}$ for all galaxies (top) and galaxies with $\log(M_*) > 10.0$ (bottom). The vertical blue line indicates the kinematic asymmetry cutoff $\overline{v_{\rm asym}} > 0.065$. Medians for normal (solid) and kinematically asymmetric (dashed) galaxies are shown in red. We see a 0.081 ± 0.03 offset in median $\frac{r_{50,{\rm H}\alpha}}{r_{50,{\rm cont}}}$ for all galaxies and 0.27 ± 0.07 offset for high-mass galaxies, as well as an overall inverse correlation between $\overline{v_{\rm asym}}$ and $\frac{r_{50,{\rm H}\alpha}}{r_{50,{\rm cont}}}$ in both cases. In the bottom panel, binned medians of $\overline{v_{\rm asym}}$ as a function of $\frac{r_{50,{\rm H}\alpha}}{r_{50,{\rm cont}}}$ are shown in magenta, further demonstrating the downward trend. Vertical error bars show the error on the median and horizontal bars show the extend of the bins in $\log(\overline{v_{\rm asym}})$.

to galaxies with $\log(M_*) > 10.0$ (Fig. 20, bottom panel), the offset in median $\frac{r_{50,{\rm H}\alpha}}{r_{50,{\rm cont}}}$ increases to 0.24 ± 0.07 and the Spearman's rank correlation test yields an even stronger result, with $\rho = -0.39$ and p-value $= 1.9 \times 10^{-5}$. The reduction in p-value is particularly notable, given that the stellar mass cutoff restricts the sample to 143 galaxies. The full sample, excluding AGNs, contains 320 galaxies. To further show the trend, binned medians of $\frac{r_{50,{\rm H}\alpha}}{r_{50,{\rm cont}}}$ as a function of $\overline{v_{\rm asym}}$ are shown in magenta, demonstrating the inverse correlation between $\overline{v_{\rm asym}}$ and $\frac{r_{50,{\rm H}\alpha}}{r_{50,{\rm cont}}}$. A similar relationship is seen when the sample is restricted to galaxies with $\log(M_*) < 9.0$ ($\rho = -0.19, p = 0.05$), but is not significant for mid-mass galaxies $9.0 < \log(M_*) < 10.0$ ($\rho = -0.088, p = 0.38$).

This indicates that whilst there is no significant increase in the amount of global star formation for kinematically asymmetric galaxies, there is a link between asymmetry and concentration of H α emission or central star formation. We note that AGN will have biased $\frac{r_{50,{\rm H}\alpha}}{r_{50,{\rm cont}}}$ measurements, so we excluded them from the above analysis. AGN are identified from placement on a BPT diagram (Baldwin, Phillips & Terlevich 1981) derived from comparison of the [N II]/H α and [O III]/H β ratios. That is, the line ratios from the spectra of the central 2 arcsec diameter of the AGN spectra sit above both the Kauffmann (Kauffmann et al. 2003) and Kewley (Kewley et al. 2001) lines on the BPT diagram. We briefly discuss AGN asymmetry in Section 8.

A detailed study of $\frac{r_{50,{\rm H}\alpha}}{r_{50,{\rm cont}}}$, SFR and stellar mass will be the subject of future work by the SAMI Galaxy Survey team (Schaefer at al. 2017).

7.3 Kinematic asymmetry and equivalent width of H α emission

To further investigate the increase in concentration of star formation (i.e. degree to which star formation is centralized) due to kinematic asymmetry, we consider directly the relationship between central and extended star formation for kinematically asymmetric and normal galaxies. We use the equivalent width (EW) of H α, which is approximately proportional to the SSFR. The EW is the ratio of current star formation (derived from the H α emission) to star formation in the past (from the r-band continuum emission). We considered the EW within half an effective radius (henceforth inner EW), compared with the EW outside half an effective radius to the edge of the IFU (henceforth outer EW), for kinematically asymmetric and normal galaxies. We did not fix the outer radius, as we found that effective radius was not related to kinemetric asymmetry, so there would be no systematic effects.

Fig. 21 shows histograms of the inner (top) and outer (bottom) EWs for kinematically asymmetric (red) and normal (black) galaxies, as well as the medians of the distributions in all cases. The median log(EW) for asymmetric and normal galaxies is the same for the outer EW and there is a marginally significant offset of 0.14 ± 0.07 dex in the inner EW, with the kinematically asymmetric and normal medians being 1.38 ± 0.05 and 1.24 ± 0.04, respectively (in log space). This result is similar in significance to the GAMA Survey results from SFR. A two-sample Kolmogorov–Smirnov test of the outer EWs yields a p-value of 0.66 of the null hypothesis, whereas the same test for the inner EWs yields a p-value of 0.0090. This indicates that only the distributions of inner EWs of asymmetric and normal galaxies are statistically dissimilar. Table 3 gives the offsets in the medians for the inner and total EW, respectively.

7.4 Possible causes and implications of concentration of star formation

There may be several causes for enhanced concentration of star formation in asymmetric galaxies. Ellison et al. (2013) used close pairs and post-merger remnants in the SDSS survey to demonstrate that central star formation is greater for post-merger galaxies than for pre-merger galaxies, by comparing SFR enhancement within and outside fibre measurements. This is qualitatively consistent with our results that kinematic asymmetry (a fraction of which is likely to be caused by interactions) is linked to star formation. We note that the central SSFR enhancement from asymmetry in Ellison et al. (2013) is larger than our value. This may be explained by their

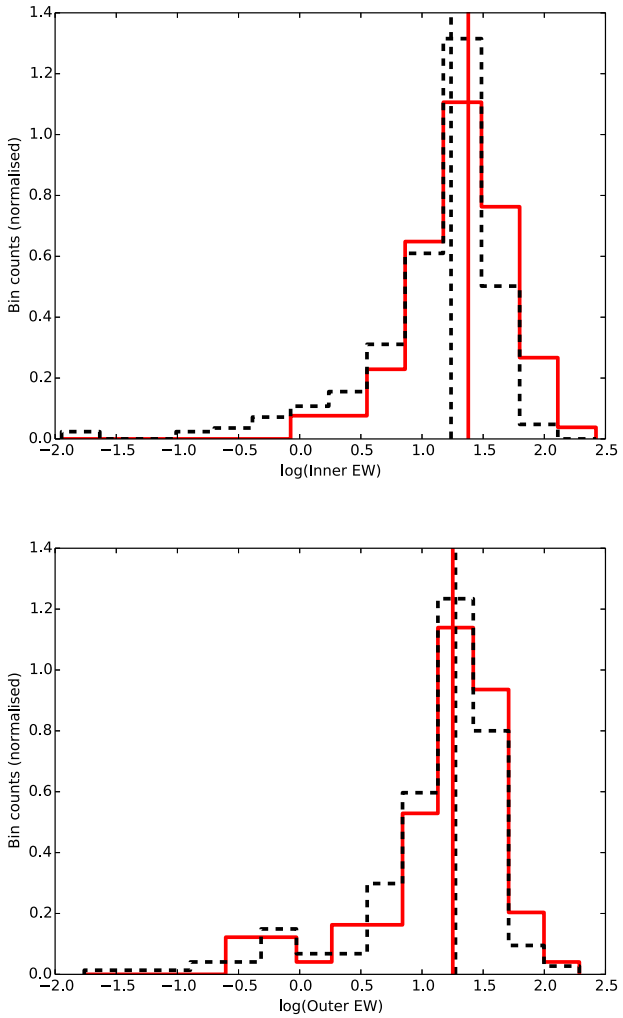

Figure 21. We show normalized histograms of the equivalent width within half an effective radius (top) and outside this range (bottom) for kinematically asymmetric (red) and normal (black, dashed) galaxies. The median equivalent widths in each case are shown for asymmetric (red, solid) and normal (black, dashed) galaxies. The medians are the same for the log(outer EW), and there is a marginally significant offset for the log(inner EW). A two-sample Kolmogorov–Smirnov test of the distributions of log(inner EW) yields a p-value of 0.0090, indicating that the distributions of log(inner EW) for kinematically asymmetric and normal galaxies are statistically dissimilar, whereas this is not the case for log(outer EW).

Table 3. Offsets in the median log(inner EW) and log(outer EW) for kinematically asymmetric and normal galaxies. There is no offset in log(outer EW), but there is an offset in log(inner EW), confirming that star formation is enhanced in the central region of asymmetric galaxies, relative to normal galaxies.

EW range	$\overline{\log(\mathrm{EW})}$ offset
Inner EW	0.14 ± 0.07 dex
Outer EW	-0.02 ± 0.16 dex

selection of galaxies in pairs, in contrast to our broader sample. A more quantitative comparison may be possible with simulated data that will more effectively isolate specific causes of asymmetry and allow for analysis of their star formation.

Barrera-Ballesteros et al. (2015) agree with our findings that there is an increase in central, but not extended star formation in interacting galaxies. They find a two to three times increase which, as in Ellison et al. (2013), is much larger than that found in this work. Their larger increase may also be explained their sample selection. They selected galaxies in interacting pairs, which excludes those that are asymmetric as a result of stochastic processes or are post-merger remnants. Our results qualitatively agree with the theoretical findings of Moreno et al. (2015), in which simulations of major mergers show an increase in central star formation, offset by suppression in the outskirts, i.e. a redistribution of gas. Further, their results indicating that lower mass galaxies exhibit greater response to the interaction may be linked to our findings of a strong inverse correlation between stellar mass and kinematic asymmetry. This will be the focus of future work.

Kaviraj (2014) also shows a positive link between star formation and morphological disturbance that they assume to be caused by minor mergers. Their enhancement values are higher than ours, with ratios of SSFR for asymmetric and normal galaxies ranging from ∼2 to ∼6, for various populations. Given that they identify asymmetric galaxies through a visual classification, to which our kinemetric method has been shown to be a good match, and use SFRs from the SDSS survey, the source of the discrepancy is not clear. Further, their asymmetric fractions of ∼10–20 per cent are broadly consistent with our results.

Given the results of Barrera-Ballesteros et al. (2015) and Moreno et al. (2015), the increased central star formation in our sample points to minor mergers as a good candidate for the source of kinematic asymmetry in a significant fraction of cases. Further, we expect minor mergers to cause, in general, lower levels of kinemetric asymmetry than major mergers, which may contribute to the difference between our distribution and the SINS Survey results in Fig. 14. In addition, the radial inflows of gas associated with minor mergers lead to the accumulation of gas in central region of the host. In some cases, nearly half of all the gas initially distributed throughout the disc forms a dense region extending several hundred parsecs in the nucleus of the galaxy (Hernquist & Mihos 1995). This may lead to nuclear starbursts, contributing to the link we see between kinematic asymmetry and central star formation.

Further, simulations show that tidal interactions can trigger repetitive central starbursts in spiral galaxies (Bekki & Couch 2011), growing the bulge and transforming them into gas-poor S0s. Such interactions may disturb the kinematics of a galaxy and lead to fluctuating star formation, causing either increased or decreased measurements of SSFR, depending on when, in the course of the interactions, the SSFR was calculated.

8 KINEMATIC ASYMMETRY OF AGN

We do not find any difference in kinematic asymmetry in AGN, compared with the general sample. The median $\overline{v_{\mathrm{asym}}}$ for the general population (excluding AGN) is 0.043 ± 0.0053 and for AGN, it is 0.048 ± 0.012. Further, a two-sample Kolmogorov–Smirnov test on the $\overline{v_{\mathrm{asym}}}$ values of AGN and non-AGN galaxies gives a probability of 0.71 of the null hypothesis, indicating that there is not a difference in distribution.

We do note that the AGN in this sample are relatively low-luminosity AGN, drawn from a mass-limited sample of regular galaxies. For a specific study of the spatially resolved kinematics of AGN, see McElroy et al. (2016).

9 CONCLUSIONS

We have defined a sample of 360 galaxies from ∼450 available in the SAMI Galaxy Survey at the start of this work.

Using a method based on kinemetry, we calculated two coefficients for each galaxy, $\overline{v_{\rm asym}}$ and $\overline{\sigma_{\rm asym}}$, which represent the median kinematic asymmetry in the velocity and velocity dispersion, respectively. We found that these coefficients, particularly $\overline{v_{\rm asym}}$, consistently distinguished between galaxies identified visually as normal or asymmetric. That is, our method and a visual classification agree for 90 per cent of visually asymmetric galaxies and 95 per cent of normal galaxies. The fraction of the sample classified as kinematically asymmetric using kinemetry was 23 per cent ± 7 per cent.

A direct comparison of our results with classification methods using the Gini, M_{20} and CAS A coefficients finds that galaxies classified as morphologically disturbed are all also kinematically asymmetric. We also find a significant population of galaxies with kinematic asymmetry that are not classified as disturbed using the Gini, M_{20} and CAS A coefficients. In contrast, a visual by-eye classification showed good agreement with the kinematic classification.

There is a strong inverse correlation between mass and kinematic asymmetry, with $\rho = -0.30$ and p-value $= 8.05 \times 10^{-8}$. Further, the proportion of galaxies classified as kinematically asymmetric falls as a function of stellar mass. This may be due to the higher gas fraction in low-mass galaxies leading to relatively larger gravitational instabilities or to the influence of environment. This result agrees with those from previous studies that have used different approaches to analyse the kinematic disturbance of low-mass galaxies.

Using SFRs from the SAMI Galaxy Survey data, we do not find a significant global offset in star formation between kinematically asymmetric and normal galaxies. However, we find that asymmetric galaxies have SFRs enhanced in their centres. We found an inverse correlation between $\overline{v_{\rm asym}}$ and the ratio between $\frac{r_{50,{\rm H}\,\alpha}}{r_{50,{\rm cont}}}$, with $\rho = -0.19$ and p-value $= 6.2 \times 10^{-4}$. If only high-mass [$\log(M_*) > 10.0$] galaxies are considered, the relationship becomes stronger, with $\rho = -0.37$ and p-value $= 6.0 \times 10^{-6}$. This indicates that kinemetric asymmetry is linked with central star formation, as has also been seen in Ellison et al. (2013) and others. A two-sample Kolmogorov–Smirnov test was able to distinguish the distributions of EWs for asymmetric and normal galaxies for inner EW only.

In future work, we shall investigate the extent to which the physical origin of kinematic asymmetry, e.g. mergers, turbulence and tidal tails, influences the results of kinemetry. Simulations will play an important role in furthering our understanding of the relationship between various kinds and magnitudes of asymmetry and the output of our kinemetric classification. We will also be able to make comparisons to high-redshift results, both through the use of simulations and artificial 'redshifting' of SAMI Galaxy Survey velocity fields. The effects of environment on disturbance will also be investigated, particularly in light of the observed mass–$\overline{v_{\rm asym}}$ relationship. The final size of the SAMI Galaxy Survey, 3400 galaxies, will also allow us to make more statistically robust statements in the future.

ACKNOWLEDGEMENTS

The SAMI Galaxy Survey is based on observations made at the Anglo-Australian Telescope. The SAMI was developed jointly by the University of Sydney and the Australian Astronomical Observatory. The SAMI input catalogue is based on data taken from the SDSS, the GAMA Survey and the VST ATLAS Survey. The SAMI Galaxy Survey is funded by the Australian Research Council Centre of Excellence for All-sky Astrophysics (CAASTRO), through project number CE110001020, and other participating institutions. The SAMI Galaxy Survey website is http://sami-survey.org/.

GAMA is a joint European-Australasian project based around a spectroscopic campaign using the AAT. The GAMA input catalogue is based on data taken from the SDSS and the UKIRT Infrared Deep Sky Survey. Complementary imaging of the GAMA regions is being obtained by a number of independent survey programs including *GALEX* MIS, VST KiDS, VISTA VIKING, *WISE*, *Herschel*-ATLAS, GMRT ASKAP providing UV to radio coverage. GAMA is funded by the STFC (UK), the ARC (Australia), the AAO, and the participating institutions. The GAMA website is http://www.gama-survey.org/.

SMC acknowledges the support of an Australian Research Council Future Fellowship (FT100100457).

LC acknowledges financial support from the Australian Research Council (DP130100664). SB acknowledges the funding support from the Australian Research Council through a Future Fellowship (FT140101166).

MSO acknowledges the funding support from the Australian Research Council through a Future Fellowship Fellowship (FT140100255).

REFERENCES

Abraham R., Tanvir N., Santiago B., Ellis R., Glazebrook K., Van Den Bergh S., 1996, MNRAS, 279, L47
Abraham R. G., Van Den Bergh S., Nair P., 2003, ApJ, 588, 218
Ahn C. P. et al., 2014, ApJ, 211, 17
Alaghband-Zadeh S. et al., 2012, MNRAS, 424, 2232
Allen J. T. et al., 2014, Astrophysics Source Code Library, record ascl:1407.006
Allen J. et al., 2015, MNRAS, 446, 1567
Amorín R., Vílchez J. M., Hägele G., Firpo V., Pérez-Montero E., Papaderos P., 2012, ApJ, 754, L22
Baldwin J. A., Phillips M. M., Terlevich R., 1981, PASP, 93, 5
Barrera-Ballesteros J. et al., 2015, A&A, 575, A45
Barton E. J., Geller M. J., Bromley B. C., van Zee L., Kenyon S. J., 2001, AJ, 121, 625
Bekki K., Couch W. J., 2011, MNRAS, 415, 1783
Brinchmann J., Charlot S., White S., Tremonti C., Kauffmann G., Heckman T., Brinkmann J., 2004, MNRAS, 351, 1151
Bryant J., O'Byrne J., Bland-Hawthorn J., Leon-Saval S., 2011, MNRAS, 415, 2173
Bryant J. J. et al., 2012, in McLean I. S., Ramsay S. K., Takami H., eds, Proc. SPIE Conf. Ser. Vol. 8446, Ground-based and Airborne Instrumentation for Astronomy IV. SPIE, Bellingham, p. 84460X
Bryant J. et al., 2015, MNRAS, 447, 2857
Burkey J. M., Keel W. C., Windhorst R. A., Franklin B. E., 1994, ApJ, 429, L13
Calzetti D., 2001, PASP, 113, 1449
Cannon J. M., McClure-Griffiths N. M., Skillman E. D., Côté S., 2004, ApJ, 607, 274
Cappellari M., Emsellem E., 2004, PASP, 116, 138
Cappellari M. et al., 2011, MNRAS, 413, 813
Casteels K. R. et al., 2013, MNRAS, 429, 1051
Casteels K. R. et al., 2014, MNRAS, 445, 1157

Charlot S., Longhetti M., 2001, MNRAS, 323, 887
Cole S., Helly J., Frenk C. S., Parkinson H., 2008, MNRAS, 383, 546
Conselice C. J., 2003, ApJS, 147, 1
Conselice C. J., Bershady M. A., Gallagher J. S., 2000, A&A, 354, L21
Conselice C. J., Bershady M. A., Dickinson M., Papovich C., 2003a, AJ, 126, 1183
Conselice C. J., Chapman S. C., Windhorst R. A., 2003b, ApJ, 596, L5
Conselice C. J., Rajgor S., Myers R., 2008, MNRAS, 386, 909
Cortese L. et al., 2014, ApJ, 795, L37
Croom S. M. et al., 2012, MNRAS, 421, 872
Darg D. et al., 2010, MNRAS, 401, 1043
De Propris R., Conselice C. J., Liske J., Driver S. P., Patton D. R., Graham A. W., Allen P. D., 2007, ApJ, 666, 212
De Propris R. et al., 2014, MNRAS, 444, 2200
Delgado R. G., Cervino M., Martins L. P., Leitherer C., Hauschildt P. H., 2005, MNRAS, 357, 945
Driver S. P. et al., 2009, Astron. Geophys., 50, 5
Eisenhauer F. et al., 2003, in Iye M., Moorwood A. F. M., eds, Proc. SPIE. Vol. 4841, Instrument Design and Performance for Optical/Infrared Ground-based Telescopes, p. 1548
Ellison S. L., Mendel J. T., Patton D. R., Scudder J. M., 2013, MNRAS, 435, 3627
Escala A., Larson R. B., 2008, ApJ, 685, L31
Fruchter A., Hook R., 2002, PASP, 114, 144
Garrido O., Marcelin M., Amram P., Balkowski C., Gach J., Boulesteix J., 2005, MNRAS, 362, 127
Geha M., Blanton M., Masjedi M., West A., 2006, ApJ, 653, 240
Gini C., 1912, in Pizetti E., Salvemini T., eds, Memorie di metodologica statistica Rome: Libreria Eredi Virgilio Veschi, 1
Glasser G. J., 1962, J. Am. Stat. Assoc., 57, 648
Glazebrook K., 2012, in Burgers J. M., Thomas R. N., eds, Proc. AIU Symp. 8, Third Symposium on Cosmical Gas Dymamics. Kluwer, Dordrecht, p. 368
Gonçalves T. S. et al., 2010, ApJ, 724, 1373
Green A. W. et al., 2014, MNRAS, 437, 1070
Hernquist L., Mihos C., 1995, ApJ, 448, 41
Hill D. T. et al., 2011, MNRAS, 412, 765
Ho I.-T. et al., 2014, MNRAS, 444, 3894
Ho I.-T. et al., 2016, MNRAS, 457, 1257
Hopkins A. M. et al., 2003, ApJ, 599, 971
Hopkins A. et al., 2013, MNRAS, 430, 2047
Huang S., Haynes M. P., Giovanelli R., Brinchmann J., Stierwalt S., Neff S. G., 2012, AJ, 143, 133
Kannappan S. J., Fabricant D. G., Franx M., 2002, AJ, 123, 2358
Kauffmann G. et al., 2003, MNRAS, 346, 1055
Kaviraj S., 2014, MNRAS, 440, 2944
Kaviraj S., Peirani S., Khochfar S., Silk J., Kay S., 2009, MNRAS, 394, 1713
Kelvin L. S. et al., 2012, MNRAS, 421, 1007
Kennicutt R. C., 1998, ApJ, 498, 541
Kewley L. J., Dopita M., Sutherland R., Heisler C., Trevena J., 2001, ApJ, 556, 121
Kirby E. N., Bullock J. S., Boylan-Kolchin M., Kaplinghat M., Cohen J. G., 2014, MNRAS, 439, 1015
Krajnović D., Cappellari M., De Zeeuw P. T., Copin Y., 2006, MNRAS, 366, 787
Krajnović D. et al., 2011, MNRAS, 414, 2923
Kutdemir E. et al., 2008, A&A, 488, 117
Lelli F., Verheijen M., Fraternali F., 2014, A&A, 566, A71
Lin L. et al., 2004, ApJ, 617, L9
Liske J. et al., 2015, MNRAS, 452, 2087
Lotz J. M., Primack J., Madau P., 2004, AJ, 128, 163
Lotz J. M. et al., 2008, ApJ, 672, 177
Lotz J. M., Jonsson P., Cox T., Croton D., Primack J. R., Somerville R. S., Stewart K., 2011, ApJ, 742, 103
Mahajan S. et al., 2015, MNRAS, 446, 2967
Markwardt C., 2009, in Bohlender D. A., Durand D., Dowler P., eds, ASP Conf. Ser. Vol. 411, Astronomical Data Analysis Software and Systems XVIII. Astron. Soc. Pac., San Francisco, p. 251
Mayer L., Kazantzidis S., Madau P., Colpi M., Quinn T., Wadsley J., 2007, Relativistic Astrophysics Legacy and Cosmology – Einstein's Legacy. Springer-Verlag, Berlin Heidelberg, p. 152
McElroy R., Croom S., Pracy M., & SAMI Galaxy Survey Team, 2016, American Astronomical Society Meeting Abstracts, 227219.02
Mihos J., Hernquist L., 1994, ApJ, 437, L47
Moreno J., Torrey P., Ellison S. L., Patton D. R., Bluck A. F., Bansal G., Hernquist L., 2015, MNRAS, 448, 1107
Neichel B. et al., 2008, A&A, 484, 159
Neistein E., Dekel A., 2008, MNRAS, 388, 1792
Noeske K. et al., 2007, ApJ, 660, L43
Pasquini L. et al., 2002, The Messenger, 110, 1
Peebles P., 1982, ApJ, 263, L1
Percival W. J. et al., 2001, MNRAS, 327, 1297
Richards S. N. et al., 2016, MNRAS, 455, 2826
Roberts M. S., Haynes M. P., 1994, ARA&A, 32, 115
Robotham A. et al., 2014, MNRAS, 444, 3986
Salim S. et al., 2007, ApJS, 173, 267
Salpeter E. E., 1955, ApJ, 121, 161
Schaefer A. L. et al., 2017, MNRAS, 464, 121
Schawinski K. et al., 2014, MNRAS, 889
Shapiro K. L. et al., 2008, ApJ, 682, 231
Sharp R. et al., 2015, MNRAS, 446, 1551
Sharples R. et al., 2013, The Messenger, 151, 21
Simons R. C., Kassin S. A., Weiner B. J., Heckman T. M., Lee J. C., Lotz J. M., Peth M., Tchernyshyov K., 2015, MNRAS, 452, 986
Stewart K. R., Bullock J. S., Barton E. J., Wechsler R. H., 2009, ApJ, 702, 1005
Stott J. P. et al., 2014, MNRAS, 443, 2695
Taylor E. N. et al., 2011, MNRAS, 418, 1587
Tully R. B., Fisher J. R., 1977, A&A, 54, 661
van Zee L., Skillman E. D., Salzer J. J., 1998, AJ, 116, 1186
Yang Y. et al., 2008, A&A, 477, 789
York D. G. et al., 2000, AJ, 120, 1579
Zucca E. et al., 2006, A&A, 455, 879 Galaxy properties and kinematic classifications

APPENDIX A: MORPHOLOGICAL AND KINEMATIC CLASSIFICATIONS, GAMA CATALOGUE INFORMATION

Table A1. Visual classification (performed by members of the SAMI Galaxy Survey team), kinemetric classification, median asymmetry in velocity dispersion and velocity, with errors, GAMA Survey catalogue values for stellar mass (Taylor et al. 2011) and colour (Hill et al. 2011) and SAMI Galaxy Survey values for SFR and $\frac{r_{50,\mathrm{H}\alpha}}{r_{50,\mathrm{cont}}}$ (Schaefer et al. 2017) for all galaxies in the sample. Where there are data missing in the SAMI Galaxy Survey values, −999.0 is the default value. The asymmetry cutoff derived in this work is $\overline{v_{\mathrm{asym}}} > 0.065$, with galaxies above the cutoff having kinemetric classification 'asymmetric' and those below it being 'normal'.

GAMA Survey ID	Vis. Class.	Kin. Class.	$\overline{v_{\mathrm{asym}}}$	$\overline{v_{\mathrm{asym}}}$ err.	$\overline{\sigma_{\mathrm{asym}}}$	$\overline{\sigma_{\mathrm{asym}}}$ err.	$\log(M_*)$	Colour $(u-r)$	log(SFR)	$\frac{r_{50,\mathrm{H}\alpha}}{r_{50,cont}}$
GAMA15218	normal	normal	0.031	0.005	0.057	0.016	9.11	1.16	0.08	0.96
GAMA15510	normal	normal	0.062	0.005	0.184	0.039	10.12	1.84	0.92	0.87
GAMA15561	perturbed	perturbed	0.111	0.019	0.448	0.338	8.19	1.16	−0.71	0.88
GAMA16026	normal	normal	0.065	0.013	0.147	0.021	10.21	1.83	1.25	0.81
GAMA16294	normal	normal	0.034	0.002	0.084	0.011	8.95	1.13	−0.36	1.04
GAMA28860	normal	normal	0.037	0.003	0.037	0.012	9.43	1.28	0.61	0.98
GAMA30377	normal	normal	0.028	0.039	0.041	0.033	8.24	1.12	−0.35	1.13
GAMA31452	normal	normal	0.053	0.004	0.071	0.015	9.43	1.17	0.49	0.89
GAMA31509	normal	normal	0.047	0.005	0.046	0.011	8.38	1.09	−999.0	0.96
GAMA31620	normal	normal	0.024	0.004	0.095	0.035	10.53	2.07	−0.11	1.26
GAMA32362	normal	normal	0.038	0.003	0.049	0.016	10.48	1.77	0.9	1.0
GAMA36894	normal	normal	0.021	0.006	0.049	0.013	8.75	1.13	−0.2	0.79
GAMA37050	normal	normal	0.031	0.007	0.089	0.021	9.15	1.41	−0.23	1.11
GAMA39108	perturbed	perturbed	0.12	0.066	0.721	0.498	8.27	1.09	−0.65	0.97
GAMA41144	normal	normal	0.021	0.0041	0.051	0.005	10.37	1.66	1.31	1.04
GAMA41164	normal	normal	0.059	0.007	0.093	0.019	8.34	0.95	−0.46	1.13
GAMA47342	normal	normal	0.03	0.003	0.032	0.019	10.05	1.61	−999.0	1.02
GAMA47500	normal	normal	0.044	0.013	0.12	0.019	9.45	1.35	0.59	0.97
GAMA47535	normal	perturbed	0.068	0.015	0.12	0.064	8.49	1.06	−999.0	0.89
GAMA49857	perturbed	perturbed	0.071	0.0042	0.10	0.015	9.14	1.12	0.58	0.83
GAMA53771	perturbed	perturbed	0.111	0.077	1.313	1.134	8.49	1.23	−999.0	0.82
GAMA53809	normal	normal	0.034	0.005	0.086	0.014	9.02	1.23	0.26	0.83
GAMA56064	normal	normal	0.048	0.012	0.115	0.071	10.51	1.88	−0.12	1.4
GAMA56140	normal	normal	0.024	0.011	0.144	0.033	11.28	2.29	1.47	0.93
GAMA56183	perturbed	perturbed	0.091	0.0052	0.12	0.013	9.44	1.27	0.41	0.83
GAMA62412	normal	normal	0.025	0.003	0.042	0.008	9.28	1.76	−0.42	0.88
GAMA62593	perturbed	normal	0.036	0.002	0.126	0.028	9.68	2.05	0.44	0.8
GAMA62718	perturbed	perturbed	0.141	0.026	0.334	0.311	9.56	1.34	1.28	0.73
GAMA64087	normal	normal	0.048	0.021	0.086	0.014	10.35	1.91	1.47	0.74
GAMA65278	normal	normal	0.043	0.034	0.096	0.022	9.09	1.31	−0.34	1.02
GAMA65406	normal	normal	0.040	0.007	0.068	0.007	11.02	2.32	0.56	0.86
GAMA65410	normal	perturbed	0.071	0.046	0.162	0.016	10.12	1.98	0.66	0.66
GAMA77445	normal	normal	0.061	0.013	0.211	0.105	8.6	1.18	−999.0	1.03
GAMA77754	normal	normal	0.022	0.004	0.116	0.016	10.49	1.51	1.66	0.81
GAMA78531	perturbed	perturbed	0.068	0.039	0.111	0.021	10.65	2.11	0.81	1.05
GAMA78667	normal	normal	0.03	0.003	0.09	0.018	10.18	1.36	−999.0	0.96
GAMA79635	normal	normal	0.03	0.002	0.041	0.039	10.44	1.61	−999.0	1.06
GAMA79693	normal	normal	0.034	0.021	0.163	0.041	10.04	2.16	−0.3	0.79
GAMA79710	perturbed	perturbed	0.07	0.064	0.266	0.043	9.0	1.53	0.22	0.86
GAMA79712	perturbed	perturbed	0.167	0.117	0.984	0.723	8.04	1.52	0.21	0.86
GAMA79771	normal	normal	0.033	0.004	0.038	0.005	8.81	1.09	−0.55	1.23
GAMA79850	normal	normal	0.052	0.021	0.098	0.007	9.81	2.07	0.37	0.66
GAMA91924	normal	perturbed	0.066	0.008	0.439	0.084	10.65	1.67	1.15	0.98
GAMA91926	normal	normal	0.024	0.003	0.181	0.027	10.09	2.25	0.16	0.78
GAMA91963	normal	normal	0.061	0.025	0.447	0.084	11.04	2.26	0.55	0.4
GAMA92770	normal	normal	0.023	0.004	0.069	0.008	9.87	1.91	−0.77	1.3
GAMA106376	normal	normal	0.041	0.017	0.097	0.026	10.17	1.21	1.43	0.94
GAMA106389	normal	normal	0.012	0.002	0.075	0.024	10.22	2.02	0.77	0.76
GAMA106717	normal	normal	0.018	0.005	0.057	0.007	10.13	1.29	1.21	1.19
GAMA137789	normal	normal	0.036	0.029	0.131	0.028	8.41	1.23	−999.0	1.02
GAMA137847	perturbed	perturbed	0.118	0.012	0.397	0.085	8.9	1.15	0.54	0.67
GAMA138066	normal	normal	0.033	0.004	0.062	0.008	9.43	2.26	0.041	0.88
GAMA138094	normal	normal	0.04	0.041	0.137	0.074	8.8	1.63	−1.01	0.71
GAMA144239	normal	normal	0.045	0.004	0.309	0.053	10.05	1.68	1.05	0.92
GAMA144243	perturbed	perturbed	0.106	0.007	0.179	0.037	8.97	1.18	−999.0	0.83
GAMA144320	normal	perturbed	0.07	0.03	0.153	0.027	10.28	1.77	1.01	0.79

Table A1 – *continued*

GAMA Survey ID	Vis. Class.	Kin. Class.	$\overline{v_{\rm asym}}$	$\overline{v_{\rm asym}}$ err.	$\overline{\sigma_{\rm asym}}$	$\overline{\sigma_{\rm asym}}$ err.	$\log(M_*)$	Colour $(u-r)$	log(SFR)	$\frac{r_{50,{\rm H}\alpha}}{r_{50,{\rm cont}}}$
GAMA144402	normal	normal	0.031	0.002	0.055	0.013	10.23	1.47	−999.0	1.01
GAMA144465	perturbed	perturbed	0.159	0.071	0.376	0.057	8.66	1.31	−1.08	0.58
GAMA144480	normal	normal	0.057	0.028	0.189	0.149	8.27	1.14	−0.6	0.82
GAMA144498	perturbed	perturbed	0.082	0.013	0.202	0.12	9.89	2.1	0.72	0.52
GAMA144682	perturbed	perturbed	0.533	0.075	0.779	0.349	8.97	1.19	−999.0	0.61
GAMA178481	normal	normal	0.052	0.005	0.101	0.037	9.06	1.29	−0.46	1.12
GAMA178578	normal	normal	0.044	0.004	0.099	0.023	8.45	1.19	−999.0	0.9
GAMA185252	normal	normal	0.05	0.008	0.128	0.027	8.55	1.23	−999.0	0.94
GAMA185291	normal	normal	0.046	0.043	0.097	0.017	8.83	1.45	−0.12	0.76
GAMA185510	normal	normal	0.046	0.005	0.074	0.018	9.38	1.57	−999.0	0.73
GAMA185532	perturbed	normal	0.052	0.004	0.096	0.02	9.14	1.34	−0.32	0.97
GAMA198503	normal	normal	0.032	0.026	0.06	0.038	8.61	1.41	−0.16	0.81
GAMA203037	perturbed	perturbed	0.116	0.091	0.731	0.282	8.23	1.22	−1.78	1.11
GAMA203114	normal	normal	0.03	0.008	0.09	0.019	10.91	2.51	0.18	0.34
GAMA203140	normal	normal	0.058	0.007	0.075	0.021	10.95	2.47	−0.9	−999.0
GAMA203148	normal	normal	0.044	0.033	0.138	0.096	9.24	1.27	0.28	1.08
GAMA204799	normal	perturbed	0.087	0.006	0.113	0.019	10.4	1.88	1.51	−999.0
GAMA204906	perturbed	perturbed	0.183	0.124	1.407	1.026	10.21	2.02	−0.18	1.51
GAMA209181	normal	normal	0.026	0.003	0.071	0.012	10.27	1.24	1.27	1.09
GAMA209319	normal	normal	0.041	0.024	0.104	0.048	8.39	0.96	0.33	0.85
GAMA209414	normal	normal	0.051	0.006	0.075	0.009	8.99	1.23	−0.31	0.85
GAMA209698	perturbed	perturbed	0.086	0.016	0.615	0.113	10.35	2.04	1.52	0.48
GAMA209701	normal	normal	0.024	0.002	0.123	0.041	10.81	2.19	0.022	1.16
GAMA209708	normal	normal	0.061	0.016	0.194	0.014	8.61	1.26	−0.53	0.99
GAMA209743	normal	normal	0.024	0.003	0.091	0.011	10.19	1.56	1.03	0.89
GAMA209807	normal	normal	0.052	0.007	0.191	0.042	10.83	1.89	1.40	0.75
GAMA215053	normal	normal	0.047	0.005	0.09	0.014	10.07	2.25	−0.62	0.61
GAMA215292	normal	normal	0.046	0.002	0.05	0.005	10.11	1.62	0.82	0.91
GAMA215335	perturbed	perturbed	0.129	0.105	0.89	0.32	10.12	1.81	1.18	0.61
GAMA215698	perturbed	perturbed	0.457	0.137	1.12	0.576	8.19	1.47	−1.35	0.65
GAMA216843	normal	normal	0.031	0.006	0.042	0.016	9.19	1.24	0.52	0.73
GAMA218713	perturbed	perturbed	0.116	0.182	0.427	0.21	10.05	2.08	0.64	0.62
GAMA220320	normal	normal	0.039	0.005	0.097	0.008	8.97	1.67	−0.52	0.35
GAMA220371	normal	normal	0.058	0.008	0.057	0.012	9.56	1.64	−0.71	1.09
GAMA220383	normal	normal	0.029	0.007	0.088	0.011	8.51	1.77	−9.0	1.511
GAMA227278	perturbed	perturbed	0.124	0.02	0.63	0.229	10.12	2.32	−0.66	0.61
GAMA227351	normal	normal	0.041	0.004	0.049	0.005	9.47	1.71	0.23	0.72
GAMA227371	normal	normal	0.045	0.007	0.111	0.076	8.53	1.13	−0.53	0.88
GAMA227407	normal	normal	0.036	0.029	0.104	0.064	8.44	1.44	−1.21	1.08
GAMA227428	normal	perturbed	0.073	0.022	0.116	0.021	9.99	1.6	0.72	0.92
GAMA227572	perturbed	perturbed	0.089	0.009	0.346	0.068	9.87	1.47	1.53	0.75
GAMA227614	perturbed	perturbed	0.098	0.032	0.381	0.033	10.01	2.02	1.2	0.69
GAMA227961	normal	normal	0.026	0.002	0.116	0.02	10.37	2.29	0.71	0.84
GAMA227970	normal	normal	0.024	0.003	0.119	0.021	10.15	1.32	1.24	0.98
GAMA228066	normal	normal	0.036	0.003	0.13	0.009	10.37	2.06	0.05	0.86
GAMA228086	perturbed	normal	0.057	0.006	0.118	0.065	9.12	1.14	−0.013	0.98
GAMA228428	normal	normal	0.046	0.002	0.05	0.011	8.85	0.77	0.68	0.81
GAMA228432	normal	normal	0.058	0.006	0.072	0.019	9.33	1.29	0.99	0.77
GAMA230714	normal	normal	0.024	0.004	0.028	0.006	10.21	1.66	1.05	1.01
GAMA230776	perturbed	perturbed	0.807	0.197	1.414	0.507	11.71	2.64	−0.43	−999.0
GAMA238080	normal	perturbed	0.065	0.035	0.401	0.201	8.26	1.12	−0.76	0.88
GAMA238085	perturbed	perturbed	0.18	0.042	0.456	0.151	9.11	1.22	−0.25	1.05
GAMA238125	normal	normal	0.037	0.004	0.045	0.009	9.56	1.57	0.74	0.76
GAMA238164	perturbed	perturbed	0.077	0.007	0.103	0.02	8.98	1.15	−0.21	0.88
GAMA238203	normal	normal	0.029	0.007	0.073	0.011	10.14	2.44	−1.17	−999.0
GAMA238204	normal	normal	0.029	0.008	0.095	0.021	10.69	1.87	−0.57	0.88
GAMA238216	normal	normal	0.046	0.03	0.143	0.023	10.17	1.81	0.71	0.68
GAMA238221	normal	normal	0.024	0.003	0.077	0.016	10.19	1.6	0.64	0.96
GAMA238276	normal	normal	0.056	0.006	0.072	0.013	10.56	2.31	−999.0	1.21

Table A1 – *continued*

GAMA Survey ID	Vis. Class.	Kin. Class.	$\overline{v_{\rm asym}}$	$\overline{v_{\rm asym}}$ err.	$\overline{\sigma_{\rm asym}}$	$\overline{\sigma_{\rm asym}}$ err.	$\log(M_*)$	Colour $(u-r)$	log(SFR)	$\frac{r_{50,{\rm H}\alpha}}{r_{50,{\rm cont}}}$
GAMA238282	normal	normal	0.039	0.005	0.081	0.014	10.59	2.14	−1.0	0.74
GAMA238328	normal	normal	0.031	0.05	0.183	0.169	8.76	1.23	0.06	0.81
GAMA238351	normal	normal	0.039	0.004	0.074	0.014	9.93	2.26	0.81	0.31
GAMA238358	normal	normal	0.043	0.004	0.099	0.075	10.86	1.73	−999.0	0.86
GAMA238360	normal	normal	0.035	0.005	0.145	0.029	10.19	2.04	0.56	0.88
GAMA238395	normal	normal	0.024	0.007	0.048	0.004	9.82	1.33	1.04	0.96
GAMA238496	normal	normal	0.043	0.008	0.136	0.024	10.2	2.21	0.61	0.55
GAMA238925	normal	normal	0.018	0.009	0.166	0.03	10.49	1.70	1.22	0.91
GAMA239172	perturbed	perturbed	0.14	0.137	0.348	0.215	8.16	1.10	−0.51	1.27
GAMA239249	normal	normal	0.019	0.025	0.037	0.005	9.34	1.61	0.13	0.81
GAMA239292	normal	normal	0.043	0.022	0.102	0.027	10.03	1.93	−0.011	0.94
GAMA239376	normal	normal	0.039	0.004	0.04	0.009	9.61	1.46	0.39	0.83
GAMA250192	normal	normal	0.051	0.006	0.085	0.02	10.71	2.39	−1.06	0.78
GAMA250277	normal	normal	0.044	0.083	0.231	0.127	9.99	1.35	1.23	0.53
GAMA272831	normal	normal	0.064	0.012	0.208	0.033	11.12	2.36	0.89	0.94
GAMA278643	normal	normal	0.051	0.004	0.022	0.006	9.16	1.48	−0.52	1.01
GAMA278684	normal	normal	0.013	0.018	0.056	0.056	8.07	1.27	−0.83	0.63
GAMA278702	normal	perturbed	0.088	0.048	0.822	0.307	8.27	1.16	−0.070	0.81
GAMA278741	normal	normal	0.038	0.003	0.062	0.006	9.25	1.35	0.15	0.91
GAMA278760	perturbed	normal	0.051	0.005	0.077	0.010	9.85	1.29	1.51	0.62
GAMA278787	normal	normal	0.061	0.042	0.127	0.046	9.16	1.39	−0.46	0.98
GAMA278846	normal	normal	0.055	0.029	0.195	0.118	9.52	1.57	0.33	0.74
GAMA278909	normal	normal	0.039	0.006	0.097	0.017	9.24	1.43	−0.19	1.11
GAMA278995	perturbed	perturbed	0.211	0.075	0.445	0.054	7.84	1.14	0.98	0.65
GAMA279818	normal	normal	0.04	0.010	0.082	0.022	9.4	1.28	0.47	1.01
GAMA279886	normal	normal	0.058	0.005	0.074	0.022	8.85	1.97	−2.97	−999.0
GAMA279891	normal	normal	0.053	0.031	0.164	0.132	8.02	0.97	−0.79	1.11
GAMA279917	normal	normal	0.054	0.004	0.074	0.008	9.19	1.22	0.57	0.77
GAMA279943	perturbed	perturbed	0.239	0.063	1.525	1.222	8.43	1.24	−0.48	0.80
GAMA288992	normal	normal	0.028	0.006	0.086	0.008	10.49	2.5	−1.4	0.28
GAMA289116	normal	normal	0.031	0.005	0.096	0.018	8.74	1.38	−0.58	0.93
GAMA289200	normal	normal	0.052	0.004	0.085	0.026	8.34	1.44	−0.97	0.76
GAMA296685	perturbed	perturbed	0.121	0.032	0.371	0.087	9.33	1.44	0.06	0.78
GAMA296798	perturbed	perturbed	0.585	0.137	1.675	0.787	8.36	1.21	−0.60	0.54
GAMA296829	normal	normal	0.052	0.016	0.101	0.015	10.19	1.83	0.19	0.78
GAMA296847	normal	normal	0.025	0.003	0.042	0.024	9.16	1.4	−0.86	0.95
GAMA296848	normal	normal	0.042	0.011	0.173	0.077	8.35	1.12	−0.8	0.86
GAMA296934	normal	normal	0.04	0.04	0.141	0.058	10.21	1.61	1.65	0.71
GAMA297557	perturbed	perturbed	0.084	0.041	0.319	0.041	8.42	1.4	−0.59	0.84
GAMA297667	normal	normal	0.032	0.003	0.041	0.007	10.25	1.77	0.94	0.93
GAMA297705	normal	normal	0.037	0.003	0.059	0.035	8.69	1.46	−0.95	0.95
GAMA300350	normal	perturbed	0.089	0.089	0.756	0.45	8.32	1.32	−1.33	1.12
GAMA300372	normal	perturbed	0.071	0.058	0.212	0.107	9.15	1.39	0.11	0.92
GAMA300477	normal	normal	0.054	0.023	0.075	0.036	9.23	1.31	−0.08	1.18
GAMA301098	perturbed	perturbed	0.295	0.208	0.415	0.41	7.67	0.97	−1.60	0.81
GAMA301799	normal	normal	0.043	0.025	0.094	0.029	9.87	1.79	0.34	0.85
GAMA302846	normal	normal	0.033	0.0032	0.054	0.005	9.85	1.69	−0.21	1.12
GAMA302994	normal	normal	0.042	0.006	0.093	0.024	8.79	1.44	−0.3	0.74
GAMA318936	normal	normal	0.032	0.008	0.079	0.015	8.76	1.02	0.020	0.98
GAMA319018	perturbed	perturbed	0.088	0.008	0.178	0.024	9.98	1.48	0.84	0.76
GAMA319049	normal	normal	0.047	0.008	0.08	0.015	10.06	1.91	0.29	0.88
GAMA319057	normal	normal	0.037	0.009	0.11	0.016	10.15	1.51	1.34	0.89
GAMA319059	normal	normal	0.062	0.008	0.093	0.023	10.05	2.17	−1.13	0.41
GAMA319067	normal	normal	0.035	0.006	0.097	0.018	10.95	2.21	−0.50	1.32
GAMA319070	normal	normal	0.033	0.005	0.098	0.018	10.65	2.37	−0.54	1.93
GAMA319139	normal	normal	0.035	0.006	0.065	0.007	8.56	1.08	−0.28	1.03
GAMA319150	perturbed	perturbed	0.216	0.071	1.834	0.48	8.5	1.21	−0.41	0.84
GAMA319157	normal	normal	0.035	0.006	0.074	0.015	10.21	2.27	−1.24	2.20
GAMA319197	normal	normal	0.056	0.008	0.078	0.013	10.4	2.38	1.00	0.89

Table A1 – *continued*

GAMA Survey ID	Vis. Class.	Kin. Class.	$\overline{v_{\rm asym}}$	$\overline{v_{\rm asym}}$ err.	$\overline{\sigma_{\rm asym}}$	$\overline{\sigma_{\rm asym}}$ err.	$\log(M_*)$	Colour $(u-r)$	log(SFR)	$\frac{r_{50,{\rm H}\alpha}}{r_{50,cont}}$
GAMA319243	perturbed	perturbed	0.208	0.12	0.549	0.286	8.53	1.43	−0.34	0.88
GAMA319272	normal	normal	0.032	0.007	0.336	0.229	8.51	1.17	−0.25	1.04
GAMA319381	normal	normal	0.011	0.003	0.091	0.011	10.29	1.57	0.94	0.90
GAMA319385	normal	perturbed	0.077	0.063	0.23	0.103	10.14	2.11	0.86	0.48
GAMA319400	normal	normal	0.02	0.0010	0.121	0.028	10.46	1.88	0.53	1.07
GAMA319453	normal	normal	0.019	0.0040	0.14	0.02	10.44	2.04	0.52	0.94
GAMA320068	normal	normal	0.044	0.037	0.052	0.027	9.2	1.34	0.17	0.93
GAMA322910	normal	normal	0.058	0.019	0.201	0.062	9.74	1.47	0.75	0.93
GAMA323504	normal	normal	0.04	0.008	0.067	0.025	10.99	2.06	1.10	0.59
GAMA323505	normal	normal	0.023	0.0060	0.114	0.017	9.93	1.71	0.18	0.87
GAMA323577	normal	normal	0.048	0.029	0.266	0.045	9.4	1.49	−0.57	1.10
GAMA324323	normal	normal	0.032	0.031	0.112	0.039	9.72	1.51	0.74	0.71
GAMA324351	normal	normal	0.038	0.005	0.071	0.014	10.45	2.38	−0.24	0.53
GAMA325390	normal	normal	0.032	0.0040	0.078	0.02	8.33	1.57	−1.74	0.72
GAMA345682	normal	normal	0.061	0.0060	0.052	0.013	9.28	1.42	−0.09	0.84
GAMA345820	normal	normal	0.06	0.007	0.089	0.011	10.17	2.06	−0.29	0.38
GAMA346046	normal	normal	0.058	0.0070	0.088	0.024	10.31	2.37	−9.0	1.24
GAMA346718	perturbed	perturbed	0.084	0.050	0.176	0.088	9.20	0.82	0.92	1.07
GAMA346793	normal	normal	0.024	0.003	0.053	0.007	10.31	1.56	1.13	0.93
GAMA346839	normal	normal	0.061	0.0050	0.095	0.020	10.39	2.29	−0.82	0.47
GAMA346890	normal	normal	0.025	0.0050	0.097	0.015	10.45	2.25	−1.41	1.04
GAMA346892	normal	normal	0.025	0.0040	0.068	0.014	10.29	1.55	1.07	0.78
GAMA346894	normal	normal	0.041	0.0060	0.071	0.02	10.49	2.54	−0.79	0.56
GAMA348115	normal	normal	0.054	0.0070	0.091	0.017	11.19	2.45	0.45	−999.0
GAMA348116	normal	normal	0.019	0.002	0.108	0.030	10.63	2.30	0.63	0.82
GAMA373173	normal	normal	0.024	0.006	0.082	0.016	11.06	2.6	−0.020	0.18
GAMA373202	normal	normal	0.057	0.005	0.139	0.015	9.27	1.81	−0.45	1.04
GAMA373284	perturbed	perturbed	0.071	0.013	0.132	0.016	9.89	1.95	0.62	0.89
GAMA375402	perturbed	perturbed	0.159	0.009	0.2	0.115	8.44	1.27	−0.43	0.91
GAMA375531	perturbed	perturbed	0.082	0.009	0.13	0.013	9.19	0.77	−9.0	0.74
GAMA376001	normal	normal	0.016	0.03	0.137	0.118	10.31	1.97	−0.070	1.04
GAMA376121	normal	normal	0.031	0.006	0.051	0.005	11.08	2.18	0.23	1.25
GAMA376185	normal	normal	0.027	0.017	0.077	0.095	9.02	1.18	−0.23	1.22
GAMA377962	normal	normal	0.019	0.052	0.047	0.076	9.05	1.33	0.09	0.76
GAMA381159	normal	normal	0.025	0.009	0.065	0.012	9.99	2.03	0.48	0.86
GAMA381207	normal	normal	0.036	0.005	0.073	0.014	10.56	2.43	−9.0	1.46
GAMA381215	normal	normal	0.033	0.008	0.141	0.027	10.4	2.46	1.01	0.65
GAMA381225	normal	normal	0.045	0.004	0.073	0.012	10.18	1.65	0.95	0.92
GAMA381229	normal	normal	0.053	0.006	0.096	0.014	10.47	2.33	−0.89	2.42
GAMA382152	perturbed	perturbed	0.088	0.006	0.138	0.051	10.19	1.67	0.49	1.05
GAMA382158	normal	normal	0.056	0.004	0.085	0.011	10.49	2.37	−0.96	0.99
GAMA383259	perturbed	perturbed	0.071	0.008	0.375	0.062	10.77	1.73	1.81	0.72
GAMA383283	normal	normal	0.016	0.001	0.067	0.012	9.2	1.70	−0.44	1.01
GAMA383318	normal	normal	0.041	0.004	0.206	0.022	9.88	1.38	0.97	0.78
GAMA386268	normal	normal	0.053	0.005	0.092	0.013	11.0	2.48	−0.24	0.33
GAMA388451	normal	normal	0.051	0.004	0.072	0.010	8.46	1.26	−0.74	0.93
GAMA388476	normal	normal	0.022	0.019	0.156	0.064	10.47	2.18	−0.38	1.05
GAMA388552	normal	normal	0.042	0.007	0.084	0.009	11.01	2.46	0.03	0.28
GAMA388603	normal	normal	0.029	0.002	0.043	0.004	9.82	1.50	0.39	0.98
GAMA417392	normal	normal	0.04	0.006	0.081	0.006	8.84	1.16	−0.19	1.08
GAMA417424	normal	normal	0.034	0.003	0.039	0.008	9.33	1.41	−0.020	0.98
GAMA417678	perturbed	perturbed	0.065	0.032	0.097	0.03	10.05	1.91	1.71	0.72
GAMA419632	normal	normal	0.051	0.046	0.038	0.065	8.91	1.62	−0.98	1.01
GAMA422320	normal	normal	0.027	0.006	0.058	0.009	9.45	1.22	0.11	0.96
GAMA422355	normal	normal	0.05	0.007	0.074	0.013	9.28	1.34	−0.56	1.06
GAMA422359	normal	normal	0.045	0.025	0.128	0.011	10.1	1.75	1.04	0.69
GAMA422366	normal	normal	0.035	0.003	0.038	0.007	9.69	1.39	0.31	1.00
GAMA422683	perturbed	perturbed	0.121	0.073	1.239	0.457	8.47	1.30	−0.13	0.86
GAMA422721	normal	normal	0.046	0.035	0.253	0.115	8.54	1.30	−1.04	0.70

Table A1 – *continued*

GAMA Survey ID	Vis. Class.	Kin. Class.	$\overline{v_{\rm asym}}$	$\overline{v_{\rm asym}}$ err.	$\overline{\sigma_{\rm asym}}$	$\overline{\sigma_{\rm asym}}$ err.	$\log(M_*)$	Colour $(u-r)$	log(SFR)	$\frac{r_{50,{\rm H}\alpha}}{r_{50,{\rm cont}}}$
GAMA422888	normal	normal	0.052	0.04	0.061	0.032	8.36	1.36	−0.92	−999.0
GAMA422907	perturbed	perturbed	0.121	0.007	0.27	0.054	9.14	1.23	0.62	1.05
GAMA422921	normal	normal	0.055	0.035	0.191	0.057	8.14	1.04	−1.12	0.99
GAMA422933	normal	normal	0.026	0.007	0.071	0.005	10.12	1.98	0.95	0.75
GAMA485504	normal	normal	0.021	0.014	0.076	0.028	10.24	1.62	0.53	1.00
GAMA485690	perturbed	perturbed	0.199	0.010	0.306	0.047	10.14	2.06	1.18	0.63
GAMA485885	normal	normal	0.036	0.004	0.047	0.016	10.28	1.71	1.03	0.8
GAMA485924	normal	normal	0.022	0.002	0.064	0.015	10.44	1.72	0.41	1.41
GAMA486872	normal	normal	0.026	0.004	0.054	0.015	10.46	1.76	0.62	1.13
GAMA486957	normal	normal	0.018	0.005	0.058	0.021	10.86	1.69	1.43	1.09
GAMA487010	normal	normal	0.055	0.03	0.283	0.043	8.98	1.30	−999.0	0.97
GAMA487027	perturbed	perturbed	0.073	0.003	0.15	0.016	9.98	1.48	1.66	0.74
GAMA492384	normal	normal	0.055	0.039	0.197	0.015	10.48	1.87	1.41	0.56
GAMA493621	normal	normal	0.036	0.006	0.060	0.009	8.98	1.17	−0.27	1.27
GAMA493811	normal	normal	0.064	0.053	0.089	0.211	8.71	1.24	−999.0	0.72
GAMA493825	perturbed	perturbed	0.159	0.081	1.014	0.367	8.27	1.20	−0.75	1.00
GAMA496966	normal	normal	0.043	0.006	0.062	0.005	10.37	1.91	0.84	0.85
GAMA504713	normal	normal	0.033	0.004	0.046	0.013	10.46	1.43	1.22	0.98
GAMA504882	normal	normal	0.027	0.031	0.073	0.059	10.15	1.84	−0.05	1.05
GAMA504922	normal	normal	0.038	0.010	0.066	0.044	10.03	1.96	0.17	0.75
GAMA505979	normal	normal	0.024	0.003	0.064	0.009	9.74	1.37	0.56	0.95
GAMA508414	perturbed	perturbed	0.093	0.016	0.139	0.015	9.63	1.45	0.84	0.69
GAMA508421	normal	normal	0.035	0.005	0.059	0.017	10.42	1.93	1.11	0.86
GAMA508480	normal	normal	0.011	0.048	0.046	0.158	9.67	1.78	0.27	0.46
GAMA508481	normal	normal	0.033	0.017	0.078	0.027	10.0	1.69	−999.0	1.05
GAMA508682	perturbed	perturbed	0.108	0.081	0.736	0.703	7.87	0.99	0.05	0.86
GAMA509557	perturbed	perturbed	0.113	0.095	0.685	0.387	8.62	1.27	0.45	0.74
GAMA509576	perturbed	perturbed	0.157	0.011	0.425	0.189	7.93	0.83	−0.72	1.3
GAMA509670	perturbed	normal	0.056	0.008	0.171	0.059	8.75	1.06	−0.27	1.28
GAMA509727	perturbed	perturbed	0.081	0.055	0.28	0.138	8.95	1.31	−0.12	1.01
GAMA511789	normal	normal	0.027	0.002	0.097	0.011	8.81	0.99	0.44	0.87
GAMA511863	normal	normal	0.044	0.015	0.093	0.023	9.37	2.03	−0.26	0.48
GAMA511867	normal	normal	0.019	0.002	0.082	0.013	10.68	1.63	1.33	−999.0
GAMA514260	perturbed	perturbed	0.076	0.006	0.238	0.015	8.9	1.56	0.26	0.73
GAMA517070	normal	normal	0.023	0.003	0.054	0.022	10.17	1.49	0.54	1.05
GAMA517164	normal	normal	0.028	0.005	0.042	0.023	10.45	1.92	−0.32	1.39
GAMA517302	perturbed	perturbed	0.125	0.072	0.234	0.18	10.26	2.05	1.08	0.4
GAMA517594	normal	normal	0.049	0.007	0.093	0.018	8.95	1.32	0.38	0.94
GAMA522127	perturbed	perturbed	0.22	0.020	1.864	0.501	8.36	1.12	−0.80	1.00
GAMA522166	normal	normal	0.05	0.009	0.175	0.206	8.83	1.09	0.29	0.91
GAMA534654	normal	normal	0.033	0.016	0.075	0.009	10.32	1.66	0.80	0.85
GAMA534655	perturbed	perturbed	0.237	0.106	1.161	0.37	11.13	2.58	0.010	0.46
GAMA534710	normal	normal	0.035	0.017	0.132	0.011	9.14	1.54	0.42	0.77
GAMA534753	normal	normal	0.035	0.004	0.117	0.015	9.56	1.59	1.76	0.5
GAMA534759	perturbed	perturbed	0.145	0.061	1.025	0.993	9.49	1.60	−0.49	0.93
GAMA536625	normal	normal	0.062	0.008	0.091	0.053	10.27	1.87	0.41	0.94
GAMA536626	normal	normal	0.056	0.005	0.079	0.007	8.91	1.04	0.32	0.94
GAMA537163	perturbed	perturbed	0.086	0.018	0.189	0.145	8.11	1.04	−0.37	1.02
GAMA537171	normal	normal	0.036	0.024	0.12	0.028	9.36	1.63	−0.17	0.98
GAMA537187	normal	normal	0.038	0.008	0.045	0.005	9.24	1.32	0.14	0.85
GAMA537367	normal	normal	0.058	0.147	0.703	0.36	9.14	1.41	0.44	0.81
GAMA537417	normal	normal	0.039	0.005	0.125	0.031	8.91	1.17	−0.59	1.13
GAMA543752	perturbed	perturbed	0.094	0.081	0.349	0.04	8.89	1.12	−0.040	1.13
GAMA543763	normal	normal	0.028	0.003	0.114	0.012	8.45	1.11	−999.0	1.08
GAMA543769	perturbed	normal	0.06	0.005	0.145	0.033	8.37	1.05	−999.0	0.89
GAMA543812	normal	normal	0.037	0.005	0.057	0.018	9.19	1.11	−0.011	1.13
GAMA543859	normal	normal	0.015	0.002	0.045	0.005	10.74	2.14	1.09	0.95
GAMA551192	perturbed	perturbed	0.232	0.075	1.029	0.751	8.76	1.38	−0.30	0.75
GAMA551202	normal	normal	0.032	0.002	0.083	0.017	9.91	1.68	1.36	0.62

Table A1 – *continued*

GAMA Survey ID	Vis. Class.	Kin. Class.	$\overline{v_{\rm asym}}$	$\overline{v_{\rm asym}}$ err.	$\overline{\sigma_{\rm asym}}$	$\overline{\sigma_{\rm asym}}$ err.	$\log(M_*)$	Colour $(u-r)$	log(SFR)	$\frac{r_{50,{\rm H}\alpha}}{r_{50,{\rm cont}}}$
GAMA558861	normal	normal	0.035	0.006	0.047	0.006	8.52	1.44	−0.85	1.11
GAMA558887	normal	normal	0.037	0.025	0.069	0.045	8.80	1.23	−0.04	0.81
GAMA561856	normal	normal	0.044	0.003	0.073	0.023	10.06	1.63	0.16	1.20
GAMA567545	normal	normal	0.038	0.004	0.098	0.032	10.93	2.08	0.91	1.14
GAMA567624	normal	normal	0.024	0.003	0.030	0.008	9.31	1.33	0.11	0.92
GAMA567676	perturbed	perturbed	0.159	0.02	0.503	0.077	8.52	1.23	−0.22	1.37
GAMA567678	normal	perturbed	0.079	0.017	0.075	0.016	9.47	2.17	−0.25	0.77
GAMA567736	perturbed	perturbed	0.223	0.015	0.45	0.102	8.47	0.64	0.32	0.99
GAMA567750	perturbed	perturbed	0.391	0.092	6.925	4.161	8.22	1.18	−0.52	−999.0
GAMA567876	perturbed	perturbed	0.107	0.074	0.76	0.755	8.27	1.33	−1.05	−999.0
GAMA567983	normal	normal	0.042	0.008	0.169	0.033	8.43	1.13	−999.0	1.00
GAMA570206	perturbed	perturbed	0.131	0.023	0.518	0.061	10.58	2.25	−0.012	0.56
GAMA570227	normal	normal	0.043	0.004	0.107	0.03	10.7	2.31	0.59	0.64
GAMA574200	normal	normal	0.035	0.005	0.086	0.021	9.35	1.25	0.73	0.97
GAMA583443	normal	normal	0.026	0.063	0.057	0.017	8.86	1.25	−0.27	1.04
GAMA592401	normal	normal	0.049	0.018	0.023	0.18	8.26	1.11	−999.0	−999.0
GAMA592421	normal	normal	0.033	0.005	0.113	0.019	10.9	1.91	1.36	1.02
GAMA592466	normal	normal	0.038	0.009	0.21	0.018	8.31	0.95	−0.38	0.89
GAMA592542	perturbed	perturbed	0.242	0.073	0.875	0.353	8.35	1.19	−999.0	1.00
GAMA592621	perturbed	normal	0.021	0.002	0.214	0.023	10.23	1.28	1.72	0.97
GAMA592835	normal	normal	0.059	0.004	0.069	0.003	10.36	1.68	1.21	0.98
GAMA592863	normal	normal	0.043	0.004	0.108	0.03	9.55	1.46	0.21	0.87
GAMA593645	normal	normal	0.056	0.012	0.258	0.024	8.53	1.20	−0.23	0.79
GAMA593680	normal	normal	0.026	0.013	0.053	0.011	10.42	2.14	0.98	0.87
GAMA594906	normal	normal	0.04	0.011	0.124	0.014	9.7	1.34	1.05	0.87
GAMA594986	normal	normal	0.023	0.019	0.088	0.007	10.12	2.18	0.55	0.77
GAMA594990	perturbed	normal	0.039	0.051	0.17	0.048	10.37	2.16	0.58	0.46
GAMA595027	normal	normal	0.027	0.004	0.042	0.005	9.86	1.63	1.10	0.85
GAMA595060	normal	normal	0.025	0.002	0.068	0.012	10.38	1.72	−0.31	1.21
GAMA599582	perturbed	perturbed	0.079	0.006	0.185	0.076	10.7	1.91	0.86	1.03
GAMA599761	normal	normal	0.022	0.005	0.075	0.013	10.93	2.10	−0.1	−999.0
GAMA599839	normal	normal	0.03	0.007	0.077	0.072	9.68	1.88	0.38	0.83
GAMA599873	normal	normal	0.035	0.022	0.173	0.11	8.89	1.29	0.020	0.88
GAMA599877	normal	normal	0.056	0.052	0.191	0.02	10.3	2.23	0.050	0.69
GAMA600014	perturbed	perturbed	0.095	0.006	0.223	0.029	8.98	1.11	0.24	0.96
GAMA600026	normal	normal	0.048	0.006	0.03	0.029	10.17	1.46	1.2	1.00
GAMA600030	normal	normal	0.046	0.008	0.153	0.027	10.25	2.12	1.41	1.30
GAMA617945	normal	normal	0.036	0.03	0.165	0.105	8.38	1.09	−999.0	1.00
GAMA618071	normal	normal	0.037	0.005	0.108	0.014	8.9	1.17	0.07	1.16
GAMA618108	normal	normal	0.043	0.007	0.185	0.015	10.45	2.47	−0.37	0.70
GAMA618116	normal	normal	0.022	0.003	0.081	0.006	10.25	1.38	1.03	1.00
GAMA618152	normal	normal	0.051	0.029	0.328	0.16	10.03	1.77	0.89	0.78
GAMA618220	normal	normal	0.046	0.003	0.067	0.037	10.62	1.98	0.10	1.15
GAMA618906	normal	normal	0.053	0.006	0.134	0.023	10.61	2.17	0.83	0.82
GAMA618935	normal	normal	0.023	0.006	0.077	0.013	9.8	1.48	0.95	0.73
GAMA618952	normal	normal	0.04	0.0050	0.205	0.034	10.79	2.38	0.030	0.97
GAMA618992	perturbed	perturbed	0.108	0.018	0.24	0.017	10.76	2.06	1.60	0.56
GAMA618993	normal	normal	0.21	0.07	0.25	0.063	10.82	1.98	2.39	0.53
GAMA618993	normal	normal	0.063	0.013	0.265	0.074	10.82	1.98	2.39	0.53
GAMA619046	normal	normal	0.037	0.0050	0.037	0.006	9.12	1.42	−0.19	−999.0
GAMA619095	normal	normal	0.024	0.0030	0.078	0.011	10.46	1.75	1.44	0.96
GAMA619097	normal	normal	0.04	0.004	0.123	0.018	9.99	1.89	0.94	0.78
GAMA619098	normal	normal	0.035	0.005	0.044	0.008	9.35	1.25	−0.00	1.06
GAMA619105	normal	normal	0.03	0.003	0.051	0.006	9.76	1.43	0.40	0.85
GAMA620034	normal	normal	0.041	0.002	0.038	0.013	10.22	1.71	0.35	0.99
GAMA620087	normal	normal	0.041	0.085	0.066	0.014	9.20	1.11	0.38	0.97
GAMA620098	normal	normal	0.042	0.004	0.156	0.024	8.97	1.08	0.22	0.78
GAMA622394	perturbed	perturbed	0.095	0.032	0.243	0.165	9.21	1.27	−0.12	1.46
GAMA622434	normal	normal	0.045	0.008	0.074	0.041	10.74	2.17	−0.12	−999.0

Table A1 – *continued*

GAMA Survey ID	Vis. Class.	Kin. Class.	$\overline{v_{\rm asym}}$	$\overline{v_{\rm asym}}$ err.	$\overline{\sigma_{\rm asym}}$	$\overline{\sigma_{\rm asym}}$ err.	$\log(M_*)$	Colour $(u-r)$	log(SFR)	$\frac{r_{50,{\rm H}\,\alpha}}{r_{50,{\rm cont}}}$
GAMA622534	normal	normal	0.027	0.007	0.042	0.009	9.12	1.38	−0.02	1.10
GAMA622694	normal	normal	0.03	0.007	0.081	0.033	10.75	1.87	1.26	0.82
GAMA622744	normal	normal	0.059	0.007	0.155	0.026	8.99	1.15	0.85	0.67
GAMA622770	normal	normal	0.062	0.049	0.097	0.052	10.02	2.07	1.12	0.65
GAMA623620	normal	normal	0.055	0.005	0.07	0.005	10.22	1.49	1.18	0.96
GAMA623641	normal	normal	0.065	0.005	0.114	0.061	9.32	1.62	−0.81	1.00
GAMA623679	normal	normal	0.04	0.003	0.071	0.008	10.19	1.78	0.29	0.96
GAMA623712	perturbed	perturbed	0.09	0.03	0.223	0.096	9.2	1.53	−0.55	0.76
GAMA623722	normal	normal	0.036	0.017	0.125	0.034	8.9	1.73	−0.96	0.85
GAMA623726	perturbed	perturbed	0.179	0.012	0.165	0.073	8.32	1.23	−1.31	0.89

This paper has been typeset from a TEX/LATEX file prepared by the author.